

1 Nanostructured and Heterostructured 2D

2 Materials for Thermoelectrics

3 Qin-Yi Li^{1,5,*}, Qing Hao^{2,*}, Tianhui Zhu³, Mona Zebarjadi^{3,4,*}, Koji Takahashi^{1,5}

4 ¹Department of Aeronautics and Astronautics, Kyushu University, Fukuoka 819-0395, Japan

5 ²Department of Aerospace & Mechanical Engineering, University of Arizona, 1130 N
6 Mountain Ave, Tucson, AZ, 85721, USA

7 ³Department of Electrical and Computer Engineering, University of Virginia, Charlottesville,
8 Virginia, 22904, USA.

9 ⁴Department of Materials Science and Engineering, University of Virginia, Charlottesville,
10 Virginia, 22904, USA.

11 ⁵International Institute for Carbon-Neutral Energy Research (WPI-I2CNER), Kyushu
12 University, Japan

13 *Corresponding authors, Qin-Yi Li: qinyi.li@aero.kyushu-u.ac.jp

14 Qing Hao: qinghao@arizona.edu

15 Mona Zebarjadi: m.zebarjadi@virginia.edu

16 Abstract

17 The rapid development in the synthesis and device fabrication of 2D materials provides new
18 opportunities for their wide applications in fields including thermoelectric energy conversion.
19 As one important research direction, the possibly poor thermoelectric performance of the
20 pristine 2D materials can be dramatically improved with patterned nanoporous structures and/or
21 heterostructures. This article reviews the recent advancement along this direction, with
22 emphasis on both fundamental understanding and practical problems.

23 **Keywords:** 2D materials, thermoelectrics, nanostructure, heterostructure

24 1. Introduction

25 Solid-state thermoelectric devices, which directly convert heat into electricity or
26 oppositely, can be utilized to address two significant issues in the development of emerging
27 micro- and nano-scale devices. One issue is how to power the ubiquitous sensors in the future
28 IoT (Internet of Things) society, where the thermoelectric power generator utilizing the
29 Seebeck effect is one of the most promising self-powering technologies to harvest energy from
30 waste heat and the environment. The second is how to dissipate the increasingly high heat flux
31 from a hot spot in the large-scale integration, where a solid-state Peltier cooler can play an
32 irreplaceable role in efficient heat removal. In the context of power generation, the performance
33 of thermoelectric material is evaluated by a well-defined dimensionless property, figure of

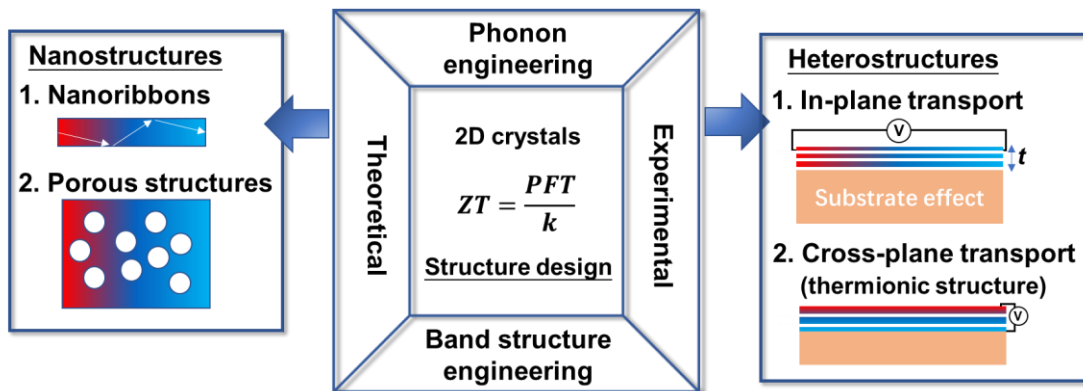
34 merit, *i.e.* $ZT = S^2\sigma T/(k_e+k_l) = PFT/k$, where $S = -\Delta V/\Delta T$ is the Seebeck coefficient
35 (thermopower), σ the electrical conductivity, T the absolute temperature; k is the thermal
36 conductivity that can be divided into the electronic part, k_e , and the lattice part, k_l ; and $PF = S^2\sigma$
37 is defined as the power factor (PF) that evaluates the ability to output a high electric power
38 with an applied temperature difference or oppositely [1]. A good thermoelectric material for
39 power generation requires a high PF , and at the same time a low k to minimize the conduction
40 heat leakage and thus maintain the temperature difference. A high ZT is also desired for a Peltier
41 refrigerator to pump heat from a cold source to a hot end. However, both a high PF and a high
42 k are beneficial in the context of thermal management where heat is transferred from a hot spot
43 to a heat sink [2]–[4]. Note that the product of PF and T , *i.e.* PFT , has the same unit with the
44 thermal conductivity of Watt per meter per Kelvin. Thus, PFT represents the ability of active
45 cooling using the Peltier effect, while k represents the ability of passive cooling [2],[5]. For
46 either power generation or thermal management, we need to manipulate S , σ , and k for improved
47 performance, which has been particularly challenging for decades because these transport
48 properties are generally intertwined.

49 There are mainly two strategies to enhance the thermoelectric figure of merit: (1) to
50 suppress phonon transport without significantly affecting electron transport, and (2) to engineer
51 the band structure for a higher PF . It is beneficial to increase the number of modes within the
52 Fermi window near the band edges, which can be realized by reducing the dimensionality
53 [6],[9]. A sharp density of states (DOS) profile at the band edge is expected in 2D materials,
54 and superior electron mobility has been observed in many 2D crystals like graphene and 2D
55 transition metal dichalcogenides (TMDCs), which is one reason why 2D materials are
56 promising for thermoelectric applications. Another advantage of 2D materials is the
57 environment-friendliness and flexibility. Traditional thermoelectric materials with $ZT > 1$
58 usually involve toxic or rare elements like Bi, Te, Pb, and Ag, which has long hindered their
59 large-scale deployment due to the high cost and environmental harm. Besides, these hard
60 materials are not suitable for energy harvesting in small-scale, flexible devices. Therefore, 2D
61 layered materials with non-toxic, low-weight, and flexible features have attracted increasing
62 attention for thermoelectric applications that are integrated into small-scale and flexible devices.

63 Many 2D materials in the pristine form indeed possess a relatively high PF . For pristine
64 graphene without doping, the Fermi level is at the Dirac point or charge neutrality point so that
65 S and $S^2\sigma$ are both zero. [27] The sign of the Seebeck coefficient is changed across the charge
66 neutrality point, where the majority charge carrier switches from electrons to holes. With an
67 applied gate voltage to optimize the Fermi level, semimetal graphene exhibits an improved
68 Seebeck coefficient of about $80 \mu\text{V/K}$ [1],[10],[11], but its PF can be up to $10 \text{ mW/m}\cdot\text{K}^2$ due
69 to the extremely high mobility [10]. Semiconducting bilayer MoS_2 can exhibit a PF up to 8.5
70 $\text{mW/m}\cdot\text{K}^2$ [12], about twice that of bulk Bi_2Te_3 . However, the figure of merit of the existing
71 pristine 2D materials is orders of magnitude lower than commercial thermoelectric materials
72 such as Bi_2Te_3 alloys. For example, the ZT value of pristine graphene [10] and 2D MoS_2 are
73 only on the order of 10^{-3} and 10^{-2} , respectively. Therefore, it is desired to independently
74 engineer both electron and phonon transport for improved thermoelectric performance of 2D
75 materials.

76 Two approaches can be used to modify the structure of a 2D system and alter the
 77 thermoelectric properties accordingly. First, a 2D sheet can be patterned into a nanostructure
 78 like a nanoribbon or a porous mesh through lithographical or special synthetic approaches. As
 79 pioneered by Hicks and Dresselhaus in 1993 [13],[14], nanostructures can alter the band
 80 structure. In later studies, suppressed phonon transport is often found as another important
 81 benefit for nanostructured materials with strong boundary or interface phonon scattering.
 82 [15],[16] For charge carriers with usually shorter mean free paths (MFPs) than those for
 83 phonons, they are less scattered so that bulk-like electrical properties can be preserved. In
 84 general, S , σ , and k can be hopefully decoupled and independently manipulated by careful
 85 structure design. Second, different 2D crystals can be stacked layer by layer to establish a van
 86 der Waals heterostructure where the band structure as well as phonon transport can be tuned by
 87 the van der Waals interfaces, promisingly leading to enhanced thermoelectric performance.
 88 Besides, the thermoelectric properties of 2D crystals can be significantly modified by the type
 89 of the substrate, and the number of layers. Up to now, researchers have exfoliated or synthesized
 90 a few dozen of 2D crystals, with at least one thousand more still waiting to be discovered
 91 [17]–[19], while the nanostructuring and stacking approaches can yield infinite possibilities for
 92 constructing a 2D system. The only limitation for tuning the thermoelectric properties is our
 93 imagination and a rational approach of the structure design.

94 In recent years, the thermoelectric studies of 2D materials have been reviewed by several
 95 articles [1],[2],[20]–[27] from different angles including an emphasis on how to tune the Fermi
 96 level. The present review is devoted to the tunability of both electron and phonon transport that
 97 is benefited from the structure manufacturability of 2D materials, including critical reviews of
 98 the most updated experimental and theoretical progress. We will start from a summary of the
 99 thermoelectric properties of pristine 2D materials, and then successively discuss the
 100 nanostructured and heterostructured 2D materials for the manipulation of thermoelectric
 101 properties and give our perspectives in the last section.



102

103

Fig. 1 Concept and outline of this review.

104 2. Thermoelectric properties of pristine 2D materials

105 In this section, the thermoelectric properties of 2D materials are reviewed. It should be
106 noted that the possibly low ZT values of these pristine materials may be largely improved with
107 the nanostructuring approach that will be discussed in later sections.

108 2.1 Thermoelectric properties of single- and few-layer graphene

109 Monolayer graphene is an intrinsic semimetal with a gapless band structure. Several
110 measurements of monolayer graphene supported on SiO_2 have confirmed a Seebeck coefficient
111 of about $80 \mu\text{V/K}$ under an optimized gate voltage to tune the Fermi level [1], [10], [11],[29],[30]
112 and an electrical conductivity on the order of 10^6 S/m at room temperature (RT) for high-quality
113 samples [10]. A high PF up to about $10 \text{ mW/m}\cdot\text{K}^2$ was reported for exfoliated single-layer
114 graphene on a suspended SiO_2 thin film, [10] which is more than twice that of commercial bulk
115 Bi_2Te_3 alloys. However, pristine graphene has an extremely high thermal conductivity of around
116 $3000 \text{ W/m}\cdot\text{K}$ in the suspended form [10]–[35] and $600 \text{ W/m}\cdot\text{K}$ in the SiO_2 -supported form [10]
117 at RT leading to a very small ZT value on the order of 10^{-3} . Here, the considerably reduced
118 thermal conductivity of the supported graphene is caused by the suppression of flexural phonons
119 from the amorphous substrate. Due to the small ZT value, large-area pristine monolayer
120 graphene is not suitable for thermoelectric power generation, but the relatively high PF and
121 remarkably high thermal conductivity can be utilized for efficient active cooling of a hot spot
122 [2].

123 Bulk graphite is also a semimetal with a high thermal conductivity up to $2000 \text{ W/m}\cdot\text{K}$. For
124 free-standing graphene, the thermal conductivity increases from the graphite value to the
125 monolayer value as the thickness decreases. However, the thermal conductivity of supported
126 graphene, which is suppressed by the substrate coupling, increases with increasing layer
127 numbers and can recover to the graphite value when the thickness is more than 30 layers [31].
128 As for the bandgap, bilayer and trilayer graphene can exhibit a nonzero bandgap and band
129 structure that can be widely tuned by the electric field or twist angle, which involves profound
130 physics [36]–[39] and can be beneficial for enhancing the Seebeck coefficient. The maximum
131 Seebeck coefficient of bilayer graphene without bandgap tuning was measured to be about 100
132 $\mu\text{V/K}$ at 250 K [40], while the maximum Seebeck coefficient of bilayer graphene gapped by
133 the electric field was reported to be up to $180 \mu\text{V/K}$ at 100 K [41],[42]. Moreover, a recent
134 theoretical work [43] reported a ZT value larger than unity in gapped bilayer graphene at an
135 ultralow temperature of 1 K .

136 2.2 Thermoelectric properties of 2D TMDCs

137 TMDCs are a family of layered materials with a molecular formula of MX_2 , where a
138 transitional metal atom, M , is sandwiched by two chalcogen element atoms, X . The 2D forms
139 of semiconducting TMDCs represented by 2H-type MX_2 ($M = \text{Mo}, \text{W}; X = \text{S}, \text{Se}$) have attracted
140 intense research efforts for their potential applications in nanoelectronics and optoelectronics
141 [44], and many studies have exploited their potentially high thermoelectric performance due to
142 their direct bandgaps and much lower thermal conductivities than that for graphene [45]–[71].

143 The thermal conductivities of bulk MoS₂ crystals have been measured to be 85–110 W/m·K
144 in the in-plane direction and 2.0 ± 0.3 W/m·K in the through-plane direction at RT using the
145 pump-probe metrology based on the magneto-optic Kerr effect [53]. A variable-spot-size time-
146 domain thermoreflectance (TDTR) approach [54] was employed to systematically measure the
147 in-plane and the through-plane thermal conductivities of bulk MX₂ (M = Mo, W; X = S, Se) at
148 80-300 K. At RT, the in-plane thermal conductivity of the measured TMDCs exhibits the
149 following decreasing order of WS₂ (120 W/m·K) > MoS₂ (82 W/m·K) > WSe₂ (42 W/m·K) >
150 MoSe₂ (35 W/m·K), the trend of which agrees well with first-principles calculations [56].
151 Another TDTR measurement of disordered, layered WSe₂ crystals yielded ultralow out-of-
152 plane thermal conductivity of 0.05 W/m·K at RT [55]. These accurate measurements of the
153 bulk crystals provide a baseline for understanding thermal transport in 2D TMDCs. The thermal
154 conductivities of single- and few-layer TMDCs have been reported by a few Raman-based
155 [57]–[63] and micro-bridge-based [64]–[66] measurements, but the limited data scattered in a
156 large range (between ~ 15 and ~ 100 W/m·K at RT for monolayer MoS₂). Meanwhile,
157 careful MD simulations [68],[50], first-principles [67] and BTE [69] calculations agreed well
158 on the in-plane thermal conductivities of 2D MoS₂, which are above 100 W/m·K for the
159 monolayer, decrease with increasing thickness and saturate at the trilayer to be about 80 W/m·K.
160 The first-principles calculations [67] reported the RT thermal conductivities of 2H-type TMDC
161 monolayers as 142 W/m·K for WS₂, 103 W/m·K for MoS₂, 54 W/m·K for MoSe₂, and 53
162 W/m·K for WSe₂. Moreover, this first-principles work found that the 1T-type TMDC
163 monolayers represented by ZrS₂ possess a much lower thermal conductivity than the 2H-type
164 monolayers [67]. Besides, Wan and co-workers [71] measured assembled TiS₂ layers with
165 organic intercalation, which exhibited an ultralow in-plane thermal conductivity of 0.12 W/m·K
166 that is two orders of magnitude lower than both bulk and monolayer TiS₂, along with a high *PF*
167 of 0.45 mW/m·K², resulting in a *ZT* value up to 0.28 at 373 K.

168 As for the *PF*, Wu and co-workers [48] measured a very large Seebeck coefficient of up to
169 30 mV/K at RT in CVD monolayer MoS₂, which indicated its promising application in
170 thermoelectrics. Hippalgaonkar and co-workers [12] measured exfoliated single- to tri-layer
171 MoS₂, and obtained a Seebeck coefficient around -400 μ V/K at a zero gate voltage, while the
172 *PF* of bilayer MoS₂ was as high as 8.5 mW/m·K² at a carrier concentration of 1.06×10^{13} /cm².
173 Another thickness-dependent study on exfoliated MoS₂/SiO₂ samples also confirms that the
174 best *PF* occurs for bilayer MoS₂. [49] In addition, Li and co-workers [51] measured tunable
175 bandgap in monolayer MoS₂ that changes with uniaxial strain at a modulation rate of up to
176 ~ 136 meV/%, thus we may expect a even larger Seebeck coefficient in deformed MoS₂ as
177 flexible thermoelectric applications. Besides MoS₂, Exfoliated 3L WSe₂ on SiO₂ shows a peak
178 Seebeck coefficient of around 200 μ V/K for electron conduction and around 250 μ V/K for hole
179 conduction at 300 K. [52] Its maximum *PF* reaches 3.7 mW/m·K² for p-type WSe₂ and about
180 3.2 mW/m·K² for n-type, corresponding to electrical conductivities of approximately 3×10^4
181 S/m and 1×10^4 S/m respectively. [52] We can combine the separately measured *PF* and
182 thermal conductivity and estimate *ZT* to be about 0.02 for pristine MoS₂ and WSe₂.

183 2.3 Thermoelectric properties of 2D black phosphorene and layered tin selenide

184 2D black phosphorus (or phosphorene) is a narrow-bandgap semiconductor with a
185 orthorhombic puckered honeycomb structure of phosphorus atoms, and has attracted great
186 attention due to its high mobility and anisotropic properties [72]. The thermoelectric properties
187 of phosphorene has attracted much attention and relatively high ZT values up to 2 have been
188 theoretically reported [77]–[83]. Tin selenide (SnSe) layers possess the same puckered lattice
189 structure and anisotropy with black phosphorus, and the layered bulk SnSe with the 2D
190 nature has been identified as one of the most high-performance thermoelectric materials with
191 an unprecedented ZT value up to 2.6 at 923 K [84]–[88]. Thus, we can group phosphorene and
192 SnSe as a family of materials with the same lattice structure that can be very promising
193 candidates as environmentally-friendly 2D thermoelectric materials.

194 The thermal conductivity of black phosphorus (BP) nanosheets has been measured by the
195 Raman optothermal method [73], time-domain thermoreflectance (TDTR) method [74], the
196 two-probe micro-bridge method [75] and the four-probe method [76]. Unlike suspended
197 graphene whose thermal conductivity increases with decreasing thickness, BP nanosheets
198 exhibited a decreasing trend of thermal conductivity in all the three directions as the thickness
199 decreases [76], which indicates that monolayer or few-layer BP can have higher ZT values than
200 thick flakes due to both enhanced electrical conductivity and reduced thermal conductivity. For
201 138–552 nm-thick BP flakes at RT, the through-plane thermal conductivity was measured to be
202 4.0 W/m·K, and the highest in-plane thermal conductivities were 86 and 34 W/mK in the zigzag
203 and armchair directions, respectively [74]. The Seebeck coefficient of 10–30 nm thick BP was
204 measured to be up to ~ 400 $\mu\text{V}/\text{K}$ near 300 K [82], and the PF of 40 nm thick BP was measured
205 to be ~ 4.5 $\mu\text{W}/\text{cm}\cdot\text{K}^2$ at 210 K [80]. Combining the experimental results of thermal conductivity
206 and PF , the ZT value of BP flakes with tens of nanometers thickness can be estimated to be on
207 the order of 10^{-3} , which indicates much room for the enhancement of thermoelectric
208 performance. As for bulk single-crystal layered SnSe, Zhao and co-workers [84] measured
209 ultralow thermal conductivities of less than 0.4 W/m·K at 923 K, Seebeck coefficients of up to
210 ~ 550 $\mu\text{V}/\text{K}$ at 300 K, and very high ZT values of larger than 2.3 at 723–973 K even without
211 doping. We can expect an even lower thermal conductivity in single- or few-layer SnSe because
212 it shares the same lattice structure with BP, and thus 2D SnSe can be a very promising
213 thermoelectric material.

214 2.4 Thermoelectric properties of other 2D sheets

215 Researchers have identified some other 2D sheets as potential good thermoelectric materials,
216 including 2D tellurium (tellurene) [90]–[92], and 2D KAgSe nanosheet [93] *etc.*, the bulk
217 counterparts of which are usually outstanding thermoelectric materials.

218 Bulk trigonal Te is a p-type narrow-bandgap semiconductor with the ZT value up to unity
219 around 600 K and ~ 0.15 at 300 K [89], and some theoretical studies [90],[91] indicated even
220 higher thermoelectric performance for the 2D counterpart of Te due to the quantum
221 confinement. Qiu and co-workers [92] measured the thermoelectric properties of 2D Te
222 nanofilms with ~ 30 -nm thickness and ~ 10 μm lateral sizes. With MEMS-based resistive
223 thermometers, the RT Seebeck coefficient and PF of the Te nanofilm sample supported on SiO_2

224 were measured to be $413 \mu\text{V}/\text{K}$ and $31.7 \mu\text{W}/\text{cm}\cdot\text{K}^2$, respectively. The thermal conductivity of
225 a suspended 2D Te sample was measured by the Raman optothermal method to be $1.5 \text{ W}/\text{m}\cdot\text{K}$,
226 half that of bulk Te. Eventually, the ZT value of ~ 30 -nm thick Te nanofilms was up to 0.63 at
227 300 K, four times that of bulk Te.

228 Besides, the thermoelectric properties of atomically thin 2D KAgSe nanosheet was studied
229 by first-principles calculations and the Boltzmann transport equation (BTE) [93], which
230 predicted an ultralow thermal conductivity of $0.03 \text{ W}/\text{m}\cdot\text{K}$ at 700 K for the trilayer KAgSe and
231 a very high ZT value up to 2.08. SnS_2 nanosheets with a thickness of several tens of nanometers
232 were measured by a MEMS-based device for the thermoelectric properties [95]. As the
233 thickness of the SnS_2 decreased, the electrical conductivity increased while the thermal
234 conductivity decreased, which leads to a ZT value up to 0.13 at 300 K, $\sim 1,000$ times that of
235 bulk SnS_2 . Shimizu and co-workers [96] measured an enhanced Seebeck coefficient in ZnO
236 thin films with a thickness of several nanometers as compared to bulk ZnO. Hung and co-
237 workers [97] conducted BTE and first-principles calculations for monolayer InSe and found a
238 PF up to $50 \text{ mW}/\text{mK}^2$. In addition, using the density functional theory (DFT) and semiclassical
239 BTE calculations, Sharma *et al.* [98] predicted enhanced ZT in As and Sb monolayers as
240 compared to the bulk counterparts, and Yu *et al.* [99] predicted a peak ZT value of 1.84 at 800 K
241 in single-layer p-type BiOBr. Wang and co-workers [110] studied another 2D carbon allotrope
242 named graphyne using the first-principles calculations and the nonequilibrium Green's function
243 (NEGF) formalism, and obtained a ZT value of 0.16 at RT that is much larger than that of
244 graphene.

245 **3. Nanostructured 2D materials for thermoelectrics**

246 As observed in Section 2, some 2D materials like graphene may not be attractive for
247 conventional thermoelectric applications. However, unfavorable properties like an ultrahigh
248 thermal conductivity can be tailored by introducing 2D nanofeatures across the atomic-thick
249 material, e.g., nanoribbons or periodic pores. This Section will summarize the major
250 advancement in this important research direction.

251 **3.1 Theoretical progress**

252 To compute the lattice thermal conductivity, two major approaches are employed for 2D
253 materials, namely first-principles calculations and molecular dynamics (MD) simulations. The
254 accuracy of MD simulations can be largely improved with first-principles computed
255 interatomic force constants [100]. Atomistic Green's function method [101],[156] can also be
256 used in certain cases based on the computed phonon transmissivity across a structure. However,
257 inelastic phonon scattering cannot be easily incorporated in this method.

258 For electrical properties, the required electronic band structures can be computed with
259 first-principles calculations (unit cell of ~ 100 atoms or less) or tight binding modeling (unit cell
260 of ~ 10 nm sizes or less). For electron conduction, both ballistic and diffuse regimes can be
261 physically formulated by the Landauer approach [6],[7], by which the spectral electrical

262 conductivity per unit energy, $\sigma'(E)$, is formulated in terms of the energy (E)-dependent
 263 transmission of electrons, $\mathcal{T}_e(E)$, given by [6]

$$\sigma'(E) = \frac{L}{A} \frac{2e^2}{h} \mathcal{T}_e(E) M_e(E) \left(-\frac{\partial f_{FD}}{\partial E}\right) \quad (1)$$

264 where $M_e(E)$ is the energy-dependent number of modes that is proportionally related to the DOS
 265 of electrons, e the electron charge, f_{FD} the Fermi-Dirac distribution function, h the Planck
 266 constant, L the sample length and A the cross-sectional area. The electron transmission function,
 267 $\mathcal{T}_e(E)$, can be related to the energy-dependent MFP, $\lambda(E)$, by $\mathcal{T}_e(E) = \lambda(E)/(\lambda(E) + L)$. [102]
 268 The total electrical conductivity is then given by

$$\sigma = \int \sigma'(E) dE \quad (2)$$

269 The Seebeck coefficient, S , is derived to be [6]

$$S = -\frac{1}{eT} \frac{\int (E - E_F) \sigma'(E) dE}{\sigma} = -\frac{1}{eT} \left[\frac{\int E \mathcal{T}_e(E) M_e(E) \left(-\frac{\partial f_{FD}}{\partial E}\right) dE}{\int \mathcal{T}_e(E) M_e(E) \left(-\frac{\partial f_{FD}}{\partial E}\right) dE} - E_F \right] \quad (3)$$

270 where E_F is the Fermi energy. Accordingly, the Seebeck coefficient is determined by the
 271 difference between the average carrier energy and the Fermi level. The Seebeck coefficient
 272 decreases while the electrical conductivity increases with increasing Fermi level, and there
 273 exists a maximum PF at the optimized Fermi level somewhere near the band edge. Further, the
 274 electronic thermal conductivity, k_e , is formulated by

$$k_e = \frac{1}{e^2 T} \int (E - E_F)^2 \sigma'(E) dE - T \sigma S^2 \quad (4)$$

275 and the lattice thermal conductivity, k_l , which dominates thermal transport in semiconductors,
 276 can be parallelly formulated by the Landauer approach in terms of the transmission function of
 277 phonons [8]. Both electron and phonon transports can be scattered by defects, impurities, and
 278 boundaries, the effects of which are reflected in the MFPs or the transmission functions of
 279 phonons and electrons in the Landauer formalism.

280 For materials like graphene and boron nitride, particular attention should also be paid to
 281 the hydrodynamics of the phonon transport [103]–[106]. This occurs when the momentum-
 282 conserving normal process overshadows the resistive Umklapp process. In contrast with bulk
 283 materials, with hydrodynamic phonon transport only at extremely low temperatures [107],
 284 phonon hydrodynamics can be found in some 2D materials well above cryogenic temperatures.
 285 Similar phonon hydrodynamics is also claimed for graphite even above 100 K [108]. In this
 286 case, heat can propagate in the form of a damped wave and second sound can be hosted within
 287 the material. This interesting phenomenon should also be considered in the thermal design of
 288 nanostructured 2D materials, such as graphene nanoribbons [109].

289 3.1.1 Nanoribbons

290 Nanoribbons are strips of 2D materials with a width of approximately less than 100 nm.
 291 Different kinds of nanoribbon structures have been studied for thermoelectric properties,
 292 including graphene nanoribbons (GNRs) of various shapes [118]–[132], sp³-bonded graphene

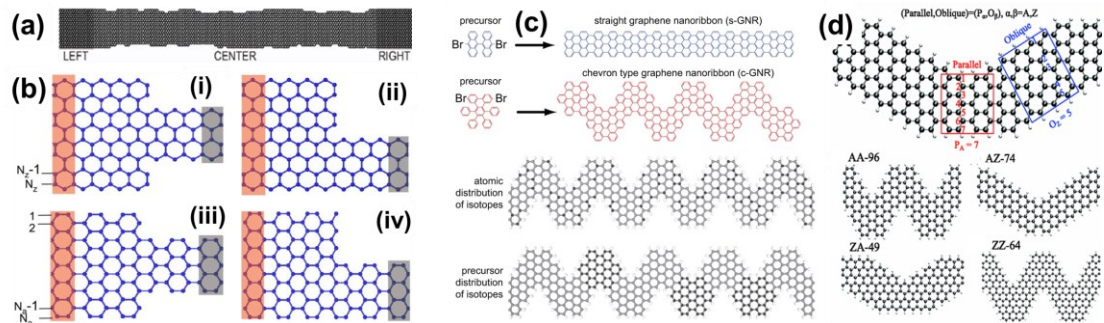
293 nanoribbons [133], silicene and germanene nanoribbons [134]-[136], TMDC nanoribbons
294 [137]-[139], phosphorene nanoribbons [140], and hybrid superlattice nanoribbons
295 [141]-[147],[134]. Table 1 lists the reported ZT values of nanoribbons in the existing
296 theoretical studies, which range from 0.1 to ~ 6 at RT.

297 All these studies reported both enhanced Seebeck coefficient due to the bandgap opening
298 and drastically reduced thermal conductivity as compared with the bulk counterpart, which can
299 be generally explained by phonon scattering with boundaries as well as the ballistic phonon
300 transport because of the nanoscale sizes that are smaller than the phonon MFP [111]-[117]. For
301 example, the phonon MFP of bulk graphene is up to ~ 300 nm [113] and thus the phonon
302 scattering with the rough edges dominates the thermal resistance in a GNR with a width of less
303 than 100 nm, while the ballistic phonon transport can be important in a GNR with a length of
304 less than 300 nm and reduce the effective thermal conductivity. Generally, the thermal
305 conductivity of nanoribbons with the same edge roughness decreases with decreasing ribbon
306 width [112]. The edge roughness is the other important factor that determines the strength of
307 phonon-edge scattering. Because the zigzag edge is more smooth than the armchair edge, which
308 suggests a weaker phonon scattering with the zigzag edge, it was found that the perfect zigzag
309 GNR has a larger thermal conductivity than the armchair ones with the same width [115],[117].
310 In practice, both experimental and theoretical studies also have demonstrated that the zigzag
311 edges also have long-termed stability [114]. For instance, the edge of a hole with more armchair
312 configuration initially would finally be stabilized with more zigzag configuration under
313 electron beam irradiation. Interestingly, phonon scattering gets much stronger at atomically
314 disordered zigzag edges of GNRs (Fig. 2 (a)), which can reduce the thermal conductivity by 10
315 fold as compared with that of perfect zigzag GNRs [119]. In addition to the phonon-edge
316 scattering, phonon scattering with isotopes [123],[124] and bulk defects [118],[120],[133] has
317 also been explored to further reduce thermal conductivity of nanoribbons. In the GNRs with
318 non-uniform widths or assembled GNRs (Fig. 2 (b)-(d)), the GNR segments can have different
319 phonon spectra and the phonon transport can be further suppressed due to the thermal boundary
320 resistance between segments as well as the phonon localization [124]-[127]. Besides, it was
321 found that the tensile strain can reduce the thermal conductivity of GNRs and thus increase the
322 ZT value [128],[129]. In the superlattice nanoribbons consisting of hybrid 2D crystals (Fig. 3
323 (b), (c) and (f), [141]-[147]), the mechanisms of thermal conductivity reduction include the
324 phonon-interface scattering and interference effects.

325 The electron transport, however, can be suppressed by the same boundary scattering as the
326 phonon transport. For the enhancement of ZT , the point is how to design a sophisticated
327 nanostructure that can suppress phonon transport much more strongly than electron transport
328 by utilizing the disparate features of phonons and electrons. Especially, defects are inevitable
329 in real samples and it is important to figure out the effects of defects on both electron and
330 phonon transport. Several theoretical studies [118]-[120] have suggested that disorders at the
331 edges can scatter phonons much more strongly than electrons in GNRs, which can lead to a
332 higher ratio of electrical to thermal conductivities and thus a higher ZT . However, bulk defects
333 inside the GNR suppress electron transport more significantly than phonons [118],[120], which
334 can result in a decreased ZT . These results suggest that a clean GNR with rough edges but few
335 bulk defects is preferred for thermoelectric applications. A more recent theoretical study [123]

336 demonstrated that isotopes and vacancies at the lowest electron density positions of GNRs can
 337 drastically reduce the thermal conductance without degrading the electrical conductance
 338 particularly in the low-energy region, which provides further guidance for sophisticated defect
 339 engineering in GNR thermoelectrics.

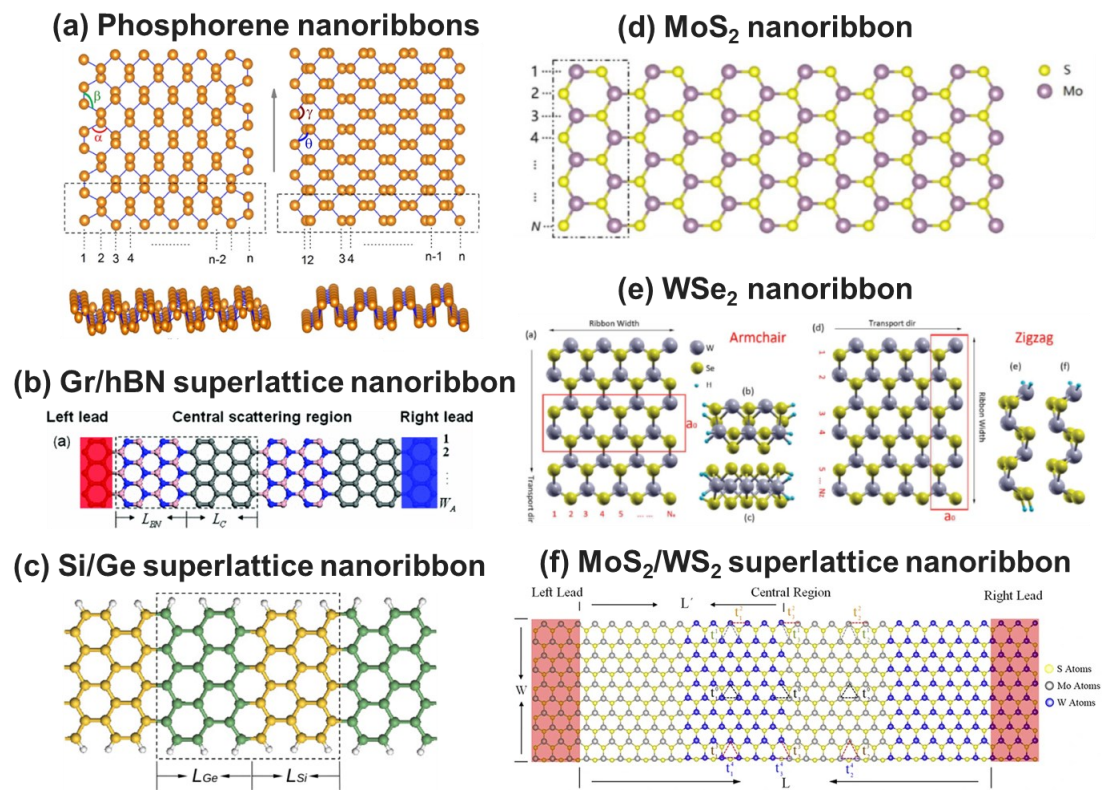
340



341

342 **Fig. 2** Graphene nanoribbon (GNR) structures for enhanced thermoelectric
 343 performance. (a) An edge disordered zigzag GNR (adapted from [119]). (b) T-shaped and
 344 L-shaped, zigzag, and armchair GNRs (adapted from [126]). (c) Precursor or isotope-
 345 based bottom-up construction of straight and chevron type GNRs (adapted from [125]).
 346 (d) GNRs assembled to various structures (adapted from [130]).

347



348

349 **Fig. 3** Various nanoribbons explored for thermoelectric applications. (a) Phosphorene
 350 nanoribbons (adapted from [140]). (b) Graphene/boron nitride superlattice nanoribbons

351 (adapted from [145]). (c) Si/Ge superlattice nanoribbons (adapted from [134]). (d) MoS₂
 352 nanoribbons (adapted from [137]). (e) WSe₂ nanoribbons (adapted from [138]). (f)
 353 MoS₂/WS₂ superlattice nanoribbon (adapted from [146]).

354

355

Table 1. *ZT* values reported in theoretical studies of nanoribbons

Material	Reference	Calculation method	Structure features	Max. <i>ZT</i>
GNR	Ouyang <i>et al.</i> (2009) [118]	NEGF	Width = 1.8 nm; varied edge disorder and vacancy	0.1 @ 300 K
GNR	Sevinçli <i>et al.</i> (2010) [119]	NEGF	Edge disordered zigzag GNRs (Fig. 2 (a))	4 @ 300 K
GNR	Karamitaheri <i>et al.</i> (2012) [121]	NEGF	Zigzag GNRs with line defects, substrate impurities & edge roughness	5 @ 300 K
GNR	Zheng <i>et al.</i> (2012) [122]	NEGF & MD	0.4-1.4 nm wide armchair and zigzag GNRs	6.0 @ 300 K
GNR	Tran <i>et al.</i> (2017) [123]	Green's function & Landauer theory	Width ~ 1 nm, isotopes & vacancies at the lowest electron density positions	2.5 @ 300 K
GNR	Tan <i>et al.</i> (2015) [124]	First-principles	Zigzag GNRs with gold atom chains at the edges	~1 @ 300 K, ~2 @ 500 K
GNR	Sevinçli <i>et al.</i> (2013) [125]	First-principles	Precursor/isotope-based straight/chevron type GNRs (Fig. 2 (c))	~2 @ 300 K 3.25@800 K
GNR	Pan <i>et al.</i> (2012) [126]	NEGF & Landauer theory	T- and L-shaped, varied chirality (Fig. 2 (b))	~0.6@300 K ~0.9@100 K
GNR	Yeo <i>et al.</i> (2013) [128]	DFT & Landauer theory	Strained armchair GNRs	~0.7@800 K
GNR	Mazzamuto <i>et al.</i> (2011) [127]	NEGF	Mixed chirality	~1 @300 K
GNR	Liang <i>et al.</i> (2012) [130]	DFT & semiempirical	GNR assembly (Fig. 2 (d))	~0.7@300 K
GNR	Mazzamuto <i>et al.</i> (2012) [131]	Green's function	Disordered edges & vacancies	0.4@300 K
GNR	Yan <i>et al.</i> (2012) [132]	NEGF	Hexagonal shapes with zigzag or armchair edges	~2@300 K
Graphane	Liang <i>et al.</i> (2009) [133]	DFT & NEGF	~1-to-5-nm wide	~2@300 K 5.8 @700 K
Silicene	Zborecki <i>et al.</i> (2013) [135]	First-principles	Zigzag edges, varied width	~2.5 @ 90 K
MoS ₂	Fan <i>et al.</i> (2014) [137]	First-principles & BTE	Varied chirality and width (Fig. 3 (d))	2.7@ 300 K
WSe ₂	Chen <i>et al.</i> (2016) [138]	First-principles	Varied chirality and width (Fig. 3 (e))	2.2 @ 300 K
WSe ₂	Wang <i>et al.</i> (2017) [139]	First-principles & NEGF & BTE	Varied chirality and sizes	1.4 @ 300 K 2.1 @ 500 K
Phosphorene	Zhang <i>et al.</i> (2014) [140]	DFT	Zigzag and armchair NRs (Fig. 3 (a))	6.4 @ 300 K

Si, Ge, and hybrid	Yang <i>et al.</i> (2014) [134]	First-principles	Varied width and supercell length (Fig. 3 (c))	2.5 @ 300 K
Gr/hBN hybrid	Tran <i>et al.</i> (2015) [143]	Green's function	hBN attached to the sides of GNRs	0.8 @ 300 K 1.0 @ 100 K
Gr/hBN hybrid	Yang <i>et al.</i> (2012) [145]	NEGF	Varied width and periodic length (Fig. 3 (b))	~0.7 @ 300 K
MoS ₂ /WS ₂ hybrid	Zhang <i>et al.</i> (2016) [146]	NEGF & MD & First-principles	Varied number of interfaces (Fig. 3 (f))	5.5 @ 600 K
TMDC hybrid	Ouyang <i>et al.</i> (2016) [147]	NEGF & MD & First-principles	Armchair MX ₂ hybrid NRs (M = Mo/W, X = S/Se)	2-3 @ 300 K 7.4 @ 800 K

356 Note: Gr = graphene

357 3.1.2 Porous structures

358 Another important type of nanostructure is the porous structure where arrays of atomic- to
359 nano-scale holes are introduced inside the 2D lattices. With tunable phonon transport and
360 electron band structures, these 2D porous structures are named as antidot lattices, nanomeshes,
361 or phononic structures [16],[148]. Several 2D porous structures have been theoretically
362 investigated for thermal, electronic and thermoelectric properties, including the most studied
363 graphene antidot lattices (GAL) [148]–[158], porous silicene [159], and 2D MoS₂ and
364 phosphorene antidot lattices [160]–[161]. On the one hand, phonon transport in these porous
365 structures can be significantly suppressed by boundary scattering and localization of phonons
366 around the pores, as well as wave-like phonon interference in periodic structures
367 [16],[152],[153]. On the other hand, the electronic band structure can be tailored in well-
368 designed porous structures so that the Seebeck coefficient can be enhanced while the electrical
369 conductivity can remain high [154]–[161]. Up to now, several theoretical studies have
370 demonstrated enhanced ZT values in 2D porous structures, as listed in Table 2.

371 GALs with nanoscale pores have been extensively studied for the electronic properties
372 [148]–[151], demonstrating a nonzero band gap around the nanopores. As for thermal transport,
373 Yang and co-workers [152] demonstrated by MD simulations that the thermal conductivity of
374 periodic graphene nanomeshes can be effectively tuned by changing the porosity and period,
375 with the thermal conductivity reduced to 0.1 to 0.01 of that of pristine graphene as the porosity
376 changed from ~21% to 65%. Feng and Ruan [153] studied thermal transport in graphene
377 nanomeshes with 5 nm neck width, 10-20 nm pore sizes, and different pore shapes and
378 arrangements using MD simulations. The thermal conductivity of the graphene nanomeshes
379 was found to be 3 orders of magnitude lower than that of pristine graphene, and even 200-fold
380 lower than that of GNRs with the same neck width, showing great potential for thermoelectric
381 applications [153]. Further, several groups reported simultaneous simulations of phonon and
382 electron transports in various graphene porous structures (or GALs), which yielded reduced
383 thermal conductivity, maintained electrical conductivity, and enhanced Seebeck coefficients
384 [154]–[158]. As listed in Table 2, the reported ZT values of GALs ranged from 0.2 to ~3.
385 Especially, Chang and co-workers [158] modified the GAL by adding adatoms, which can
386 enhance the spin-orbit coupling and thus convert bulk graphene into a topological insulator with
387 a bandgap and robust helical edge states. While phonon transport was significantly suppressed

388 by the nanopores, the Seebeck coefficient reached up to 1 mV/K and the maximum ZT value
 389 was as high as ~ 3 at 40 K [158].

390 Besides graphene porous structures, Sadeghi and co-workers [159] reported enhanced
 391 thermoelectric performance of silicene antidot lattices (Fig. 4 (d)), with the Seebeck coefficient
 392 up to 500 $\mu\text{V/K}$ and the ZT value as high as 3.5. Shao *et al.* [160] reported electronic properties
 393 of MoS_2 antidot lattices (Fig. 4 (f)) using first-principles calculations and found tunable
 394 bandgaps with the supercell sizes and the foreign atom adsorption. Cupo and co-workers [161]
 395 reported tunable band gaps of phosphorene antidot lattices (Fig. 4 (e)) both theoretically and
 396 experimentally. Their DFT calculations revealed that the bandgap scaling can be attributed to
 397 quantum confinement effects [161].

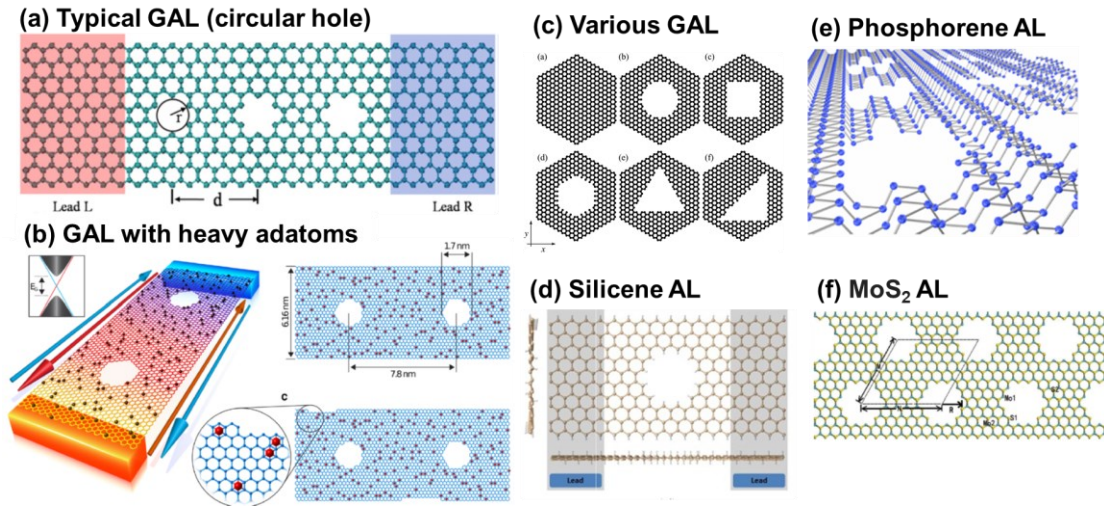
398

399

Table 2. ZT values reported in theoretical studies of 2D porous structures

Material	Reference	Calculation method	Structure features	Max. ZT
GAL	Gunst <i>et al.</i> (2011) [154]	Landauer theory	Hexagonal holes with varied sizes and edge chiralities	~ 0.3 @ 300 K
GAL	Karamitaheri <i>et al.</i> (2011) [155]	Landauer theory	Circular, rectangular, hexagonal, and triangular antidot shapes (Fig. 4 (c))	~ 0.2 @ 300 K
GAL	Yan <i>et al.</i> (2012) [156]	NEGF	1D antidot arrays (Fig. 4 (a))	~ 1.0 @ 300 K
GAL	Hossain <i>et al.</i> (2015) [157]	DFT & NEGF	Rectangular hole with varied sizes	~ 0.8 @ 300 K
GAL	Chang <i>et al.</i> (2014) [158]	First-principles	Both heavy adatoms and nanopores (Fig. 4 (b))	~ 3 @ 40 K
Porous silicene	Sadeghi <i>et al.</i> (2015) [159]	DFT	Varied doping and edge termination (Fig. 4 (d))	3.5 @ 300 K

400



401

402 **Fig. 4** 2D porous structures. (a) Typical graphene antidot lattice (GAL) with circular
 403 holes (adapted from [156]). (b) GAL with heavy adatoms (adapted from [158]). (c) GAL
 404 with holes of different geometries (adapted from [155]). (d) Silicene antidot lattice
 405 (adapted from [159]). (e) Phosphorene antidot lattice (adapted from [161]). (f) MoS₂
 406 antidot lattice (adapted from [160]).

407

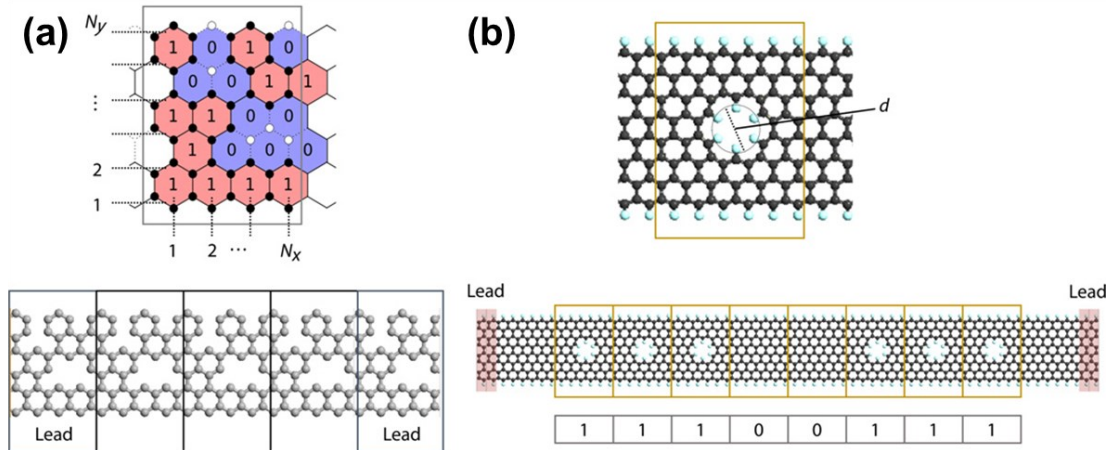
408 3.1.3 Machine learning approaches

409 As suggested in the previous sections, there are infinite possibilities for the nanostructure
 410 patterns of 2D materials, and hence the case-by-case enumerative studies towards an optimized
 411 structure for thermoelectric applications are awfully expensive, inefficient, and often
 412 unsuccessful. To address this issue, the machine learning techniques or materials informatics
 413 have recently attracted growing interest in the field of thermal transport and thermoelectric
 414 studies [162]–[166]. Combining the limited data accumulated from simulations and
 415 experiments with the data-driven machine learning or AI approaches can greatly accelerate the
 416 discovery of high-performance thermoelectric structures. Especially, some machine learning
 417 algorithms have been utilized to optimize 2D nanostructures for the target properties.
 418 Yamawaki and co-workers [162] combined phonon and electron transport calculations of
 419 graphene nanostructures with Bayesian optimization, and successfully discovered certain
 420 structure configurations that can comprehensively optimize the thermal and electrical properties
 421 towards an enhanced thermoelectric figure of merit. Two kinds of well-defined graphene
 422 nanostructures were investigated for the optimization (Fig. 5): (1) the distribution of vacancy
 423 defects, and (2) one-dimensional configuration of the antidot lattice unit and pristine unit. The
 424 optimized antidot structure exhibited the highest ZT value that is 11 times that of the pristine
 425 GNR and more five times that achieved by random search, which was attributed to the zigzag
 426 edge states and the unique aperiodic nanostructure.

427 A recent work by Wei *et al.* [163] adopted a two-step search process coupled with the
 428 genetic algorithm to answer whether the thermal conductivity of GALs with periodically
 429 distributed holes is always higher than that of GALs with randomly distributed holes. Around
 430 these random holes, the phonon Anderson localization has been believed to largely suppress

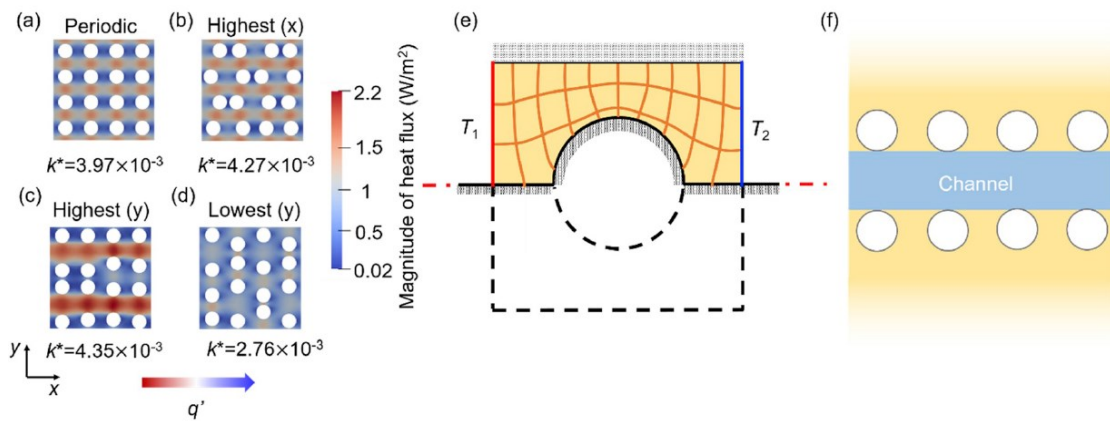
431 phonon transport. Unexpectedly, Wei and co-workers discovered certain patterns of nanopore
 432 distributions with an enhanced thermal conductivity as compared to that of periodic pore
 433 distribution (Fig. 6), which was never found during the manual search. The unexpected thermal
 434 conductivity enhancement was attributed to the shape factor and channel factor in these unusual
 435 structures that dominate over the phonon localization. This study demonstrated the possibilities
 436 and complexity of the structure-property relationship in 2D nanostructures, which can stimulate
 437 further machine-learning based optimization and provide guidance for the rational design of
 438 two-dimensional structure patterns for enhanced thermoelectric performance.

439



440
 441 **Fig. 5 Bayesian optimization for enhanced ZT of graphene nanostructures. (a)**
 442 **Optimization of the vacancy distribution (Model A). (b) Optimization of the arrangement**
 443 **of the pristine and antidot GNR cells (Model B). The descriptors, 0 and 1, respectively**
 444 **describe the defective and complete hexagonal lattices for Model A, and the pristine and**
 445 **antidot GNR cells for Model B. Adapted from [162].**

446



447
 448 **Fig. 6 Genetic algorithm (GA) driven discovery of thermal conductivity enhancement**
 449 **in disordered GALs. (a) Periodic configuration of nanopores, (b), (c) the configuration**
 450 **with the disorder in x and y direction identified by GA for high thermal conductivity, (d)**
 451 **the configuration with the disorder in y -direction identified by GA for low thermal**

452 conductivity. (e) The shape factor illustrated using a quasi-1D heat conduction model. (f)
453 Schematic of heat conduction channel. Adapted from [163].
454

455 3.2 Experimental progress

456 This section reviews the progress in experimental studies of nano-patterned 2D materials.
457 Caution should be taken for the significant knowledge gap between computations in Section
458 3.1 and the experimental studies in this section. A few issues should be addressed:

- 459 1) Band structure computed by first-principles calculations [167]–[169],[149] (unit cell
460 of ~100 atoms or less) or tight binding modeling [151],[170]–[174] (unit cell of ~10
461 nm sizes or less) often focus on pore diameters of ~1 nm or less. In addition,
462 qualitatively estimate of the band structure can be obtained by fast numerical solutions
463 of the Dirac equation [171]. In experiments, however, the smallest pore diameter is still
464 in the sub-20 nm regime due to the restriction of employed nanofabrication techniques
465 [175],[176].
- 466 2) The band gap opening is suggested to depend on the chirality of the supercell lattice
467 vectors [168],[170], which has not been verified experimentally.
- 468 3) Structure disorder (e.g. irregular pore shape) [174],[172],[169], and the exact structure-
469 edge configuration (i.e. armchair or zigzag edges) are considered in some computations
470 but no atomic structure information from real samples is available for such studies.

471 Although electrical properties can usually be accurately measured, special attention should
472 also be paid to the challenges of thermal measurements. As the most accurate approach for the
473 thermal measurements of nanostructures, the thermal conductivity of a nanostructure can be
474 obtained from steady-state and one-dimensional heat conduction along the structure. This can
475 be achieved with suspended heater-thermometer membranes [177],[178] or metal lines [200]
476 bridged by the measured nanostructure. For fragile nanoporous structures, this approach has
477 not been used though it can be found for supported graphene nanoribbons [200] and suspended
478 graphene [179],[180]. Metal deposition is often used to form good thermal/electrical contacts
479 between the sample and the suspended device. Along another line, non-contact Raman
480 thermometry can also be used to extract the in-plane thermal conductivity of a suspended 2D
481 material. The model can be either based on a self-heated suspended strip [181] or laser-heated
482 sample with circular temperature profiles from the laser spot [182],[183],[34],[202]. Besides
483 the less accurate temperature reading of Raman thermometry, accurate thermal analysis may
484 also involve the strong thermal nonequilibrium between electrons, optical phonons and acoustic
485 phonons [183],[195] in laser-heated 2D materials.

486 Keeping these in mind, reliable and systematic thermoelectric measurements should be
487 carried out with more advanced nanofabrication techniques to control the patterns at the atomic
488 level. Nevertheless, the experimental results in this section are still critical and some of the
489 materials can be useful in applications already.

490 3.2.1 Porous structures

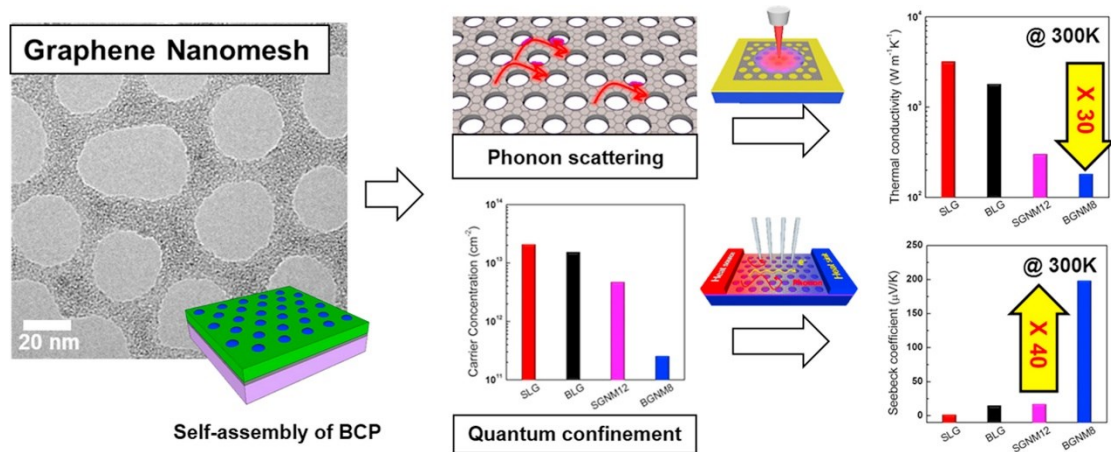
491 Despite many theoretical studies, extremely limited experiments have been carried out to
492 demonstrate the predicted thermoelectric performance of 2D nanostructures due to the
493 challenges of both sample fabrication and thermal measurements at the nanoscale.

494 The fabrication of 2D porous structures can be classified into three categories: (1)
495 chemical etching or plasma treatment to introduce random and uncontrollable holes or defects
496 [172],[191], (2) helium or gallium ion-beam based direct drilling of holes in the 2D material
497 [189],[190], and (3) mask based patterning (electron beam lithography [161],[186], or block
498 copolymer self-assembled porous mask [185]) followed by plasma etching processes. The
499 electron beam lithography-based patterning can offer the most accurate and large-scale control
500 of the nanostructure, with the smallest pore diameter around 15 nm [186]. The helium ion beam-
501 based milling yielded the smallest pore size of approximately 6 nm in diameter [191].

502 Xiao and co-workers [172] treated few-layer graphene (FLG) with oxygen plasma for
503 10–20 seconds to introduce atomic scale holes (defects). The Seebeck coefficient of the plasma-
504 treated few-layer graphene was measured to be as high as 700 $\mu\text{V}/\text{K}$ at 575 K, which was
505 attributed to the bandgap opening induced by the local holes or defects [172]. The electrical
506 conductivity of the randomly etched FLG was $\sim 10^4$ S/m, which is 2 orders of magnitude lower
507 than high-quality samples, and the PF was $4.5 \text{ mW}/\text{m}\cdot\text{K}^2$, only about half that of high-quality
508 pristine graphene. Such plasma treatment can not be used for single-layer graphene that can be
509 easily destroyed by plasma etching [172]. Similar random chemical etching was recently adopted
510 by Kang et al. [191] to introduce random holes in 7 nm-thick MoS_2 thin films, the in-plane
511 Seebeck coefficient of which was measured to be up to $\sim 742 \mu\text{V}/\text{K}$.

512 Using the block copolymer self-assembly method (Fig. 7), Oh and co-workers [185]
513 fabricated mono- and bi-layer graphene nanomeshes with irregular holes. The hole diameter in
514 the nanomeshes was about 20–40 nm, and the average neck widths were 8–21 nm. They
515 measured the Seebeck coefficient and electrical conductivity of SiO_2 -supported samples by a
516 commercial instrument (TEP-600, Seepel Instrument, Korea), and measured the effective
517 thermal conductivity of a different suspended porous graphene sample by the Raman
518 optothermal method. Note that the Raman-based measurement here can involve large
519 uncertainties due to several factors, including the unknown laser absorption and phonon
520 nonequilibrium as well as the relatively low sensitivity for temperature detection [192]–[195],
521 which we will discuss in more detail later. The bilayer graphene nanomesh with 8 nm neck
522 width exhibited the lowest thermal conductivity of about 78 W/mK around 350 K due to the
523 phonon scattering at the neck edge, and the highest Seebeck coefficient of $-190 \pm 80 \mu\text{V}/\text{K}$ at
524 300 K and $-520 \pm 92 \mu\text{V}/\text{K}$ at 520 K, which can be explained by the bandgap opening. However,
525 the electrical conductivity was significantly reduced by 2 orders of magnitude to be around 2
526 $\times 10^4$ S/m, which should be originated from the defects and contamination introduced in the
527 nanofabrication processes. Oh and co-workers achieved a PF of about $8.2 \text{ mW}/\text{m}\cdot\text{K}^2$ at 520 K
528 in the bilayer nanomesh with 8 nm neck width due to the superior Seebeck coefficient, but the
529 ZT of all the measured nanostructures were even decreased by 1–2 orders of magnitude as
530 compared to large-area graphene because the electrical conductivity was not maintained high
531 enough.

532 Although this work provided the first experimentally measured ZT for GALs, the thermal
533 contact between the sample and the thermal probes may largely affect Seebeck coefficient
534 measurements, where the measured temperature difference can be larger than that “felt” by the
535 sample. Some PF s given by Oh and co-workers [185] were suspected to be an underestimate
536 of the actual values. On the other hand, their thermal measurements used a Raman laser as a
537 heat source and read the temperature from the Raman peak shift. The laser light was focused
538 on a GAL suspended across a membrane hole. The laser spot acted as a heating source, whereas
539 the membrane was the heat sink to “drain” the heat from the suspended sample. The effective
540 thermal conductivity of a GAL was thus obtained from 2D heat conduction analysis. One
541 challenge was how to determine the actual laser power absorbed by a sample. In the work by
542 Oh *et al.*, the possible light reflection by the graphene antidot lattice was neglected and the laser
543 power not transmitted through a sample was considered to be absorbed. In addition, the in-air
544 measurements were affected by convection and air conduction around the sample, which was
545 usually hard to be estimated. More accurate measurements also required a better understanding
546 of light absorption by graphene, i.e., the strong thermal nonequilibrium between electrons,
547 optical phonons and acoustic phonons [183],[195].



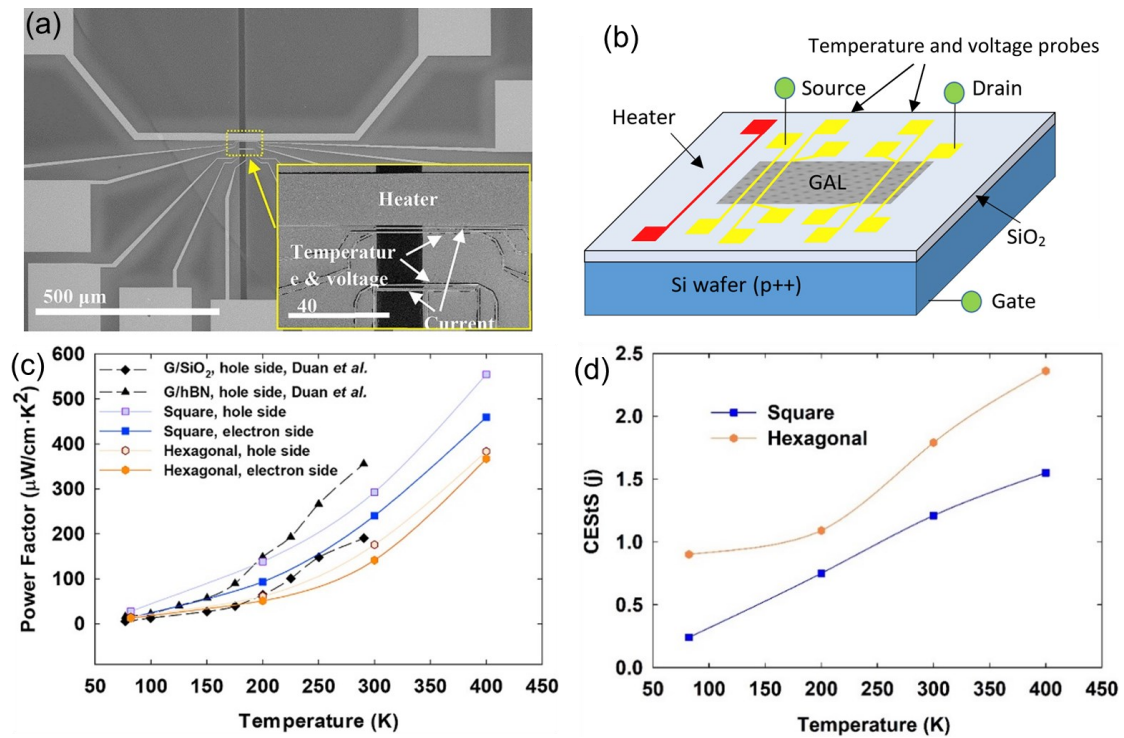
548
549 **Fig. 7 Reduced thermal conductivity and enhanced Seebeck coefficient measured in**
550 **graphene nanomeshes. Adapted from [185].**

551
552 Xu and co-workers [186] fabricated GALs by the electron beam lithography and reactive
553 ion etching. To minimize the measurement errors, deposited metallic electrical/thermal probes
554 were used to ensure good thermal/electrical contacts. The square and hexagonal patterns were
555 compared for their electrical properties. The square pattern exceeded the hexagonal pattern for
556 the PF under an gate voltage that maximized $|S|$ (Fig. 8 (c)). At 400 K, a remarkable PF of
557 $554 \mu\text{W}/\text{cm}^2\text{K}^2$ is achieved in the p-type GAL with a square pattern, which is far beyond the
558 best PF s of bulk thermoelectric materials. One innovation of this work was to better analyze
559 the maximum Seebeck coefficient under an applied gate voltage, from which the carriers’
560 energy sensitivity (j) to scattering (CEStS) was extracted to better understand the scattering
561 mechanisms of charge carriers. In physics, this CEStS is defined as $j = d[\ln(\tau)]/d[\ln \varepsilon]$,
562 where τ is energy-depdent relaxation time, ε is the carrier's energy referring to the edge of

563 the corresponding valley. The extracted j in Fig. 8 (d) reflects a statistical measure of the
 564 average values of j for all existing scattering mechanisms. Because the divergence between
 565 electrons and holes is within 10%, the averaged j value is plotted here. Here the positive j
 566 value indicates increased importance of the long-range scattering sources at elevated
 567 temperatures. This new technique can be applied to general 2D materials for better understand
 568 their electron transport processes.

569 Due to the experimental complexity, the pore-edge configuration (e.g. armchair or zigzag)
 570 was not checked in all measured samples. The pore sizes are also significantly larger than those
 571 used in computations. In this aspect, high-quality samples may be prepared by the direct growth
 572 of a nanoporous pattern with SiO_2 pillar as the mask that can be removed with hydrofluoric acid
 573 etching later. A similar study can be found for the direct growth of nanoporous $\text{In}_{0.1}\text{Ga}_{0.9}\text{N}$ films
 574 for thermal studies [187]. A more perfect structure, with an ordered inclusion of uniform holes
 575 and nitrogen atoms, can be directly synthesized. Examples can be found in C_2N -h2D crystals
 576 [239], polyaniline (C_3N) with six nitrogen atoms periodically surrounding a phenyl ring [240].
 577 Phonon studies are also carried out on monolayer C_3N structure with a periodic array of zigzag
 578 holes [188].

579



580

581 **Fig. 8** The enhanced PF of GALs and the detection of major charge-carrier scattering
 582 mechanism. (a) SEM image of the test device. (b) Schematic of the measurement
 583 principles. (c) PF s of different samples as a function of temperature. (d) The CESTS (j)
 584 of GALs with a square array and a hexagonal array of nanopores. Adapted from [186].

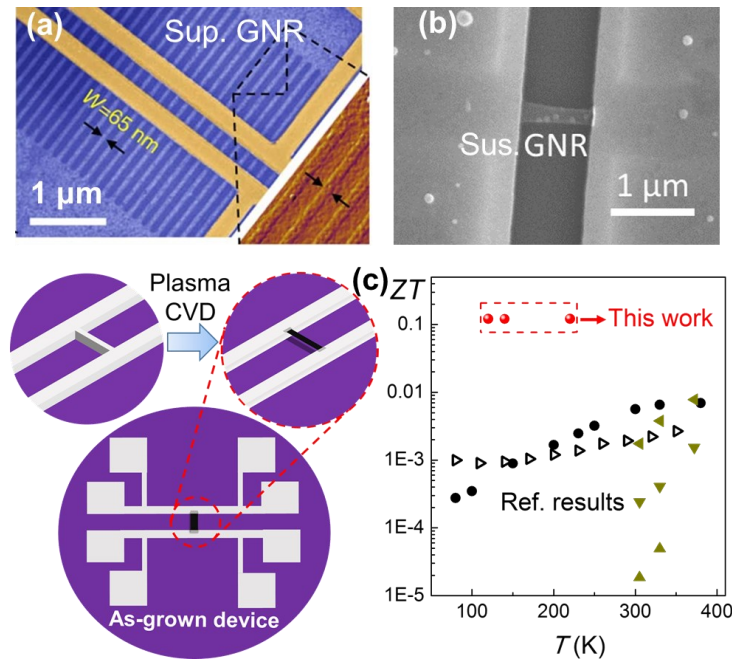
585 3.2.2 Graphene nanoribbons

586 Han and co-workers [199] first experimentally demonstrated the bandgap opening in
587 lithographically patterned GNRs in 2007. The bandgap increased from 3 meV to 300 meV as
588 the GNR width decreased from 90 nm to 15 nm [199], thus we can expect an enhanced Seebeck
589 coefficient in GNRs with a width of several tens of nanometers. Recent experimental progress
590 has also confirmed drastic reduction of thermal conductivity in both SiO₂-supported and
591 suspended GNRs (Fig. 9). Bae and co-workers [200] patterned exfoliated graphene sheets into
592 arrays of GNRs with ~260nm length and 45–130 nm widths using electron beam lithography
593 and deposited the heater and sensor on top for the thermal conductivity measurement of SiO₂-
594 supported GNRs (Fig. 9 (a)). The thermal conductivity exhibited a clear width dependence that
595 scales as $k \sim W^{1.8 \pm 0.3}$, with the room-temperature k of 65-nm-wide supported GNRs suppressed
596 to about 100 W/mK, about one-sixth of large-area supported graphene [10]. This reduction of
597 k was mainly attributed to the strong scattering between phonons and the plasma-etched rough
598 ribbon edges. Also using the lithographical patterning and plasma etching followed by substrate
599 etching, Li and co-workers [197] measured the thermal and electrical conductivities of an
600 individual suspended GNR with 169 nm width and 846 nm length (Fig. 9 (b)). The RT thermal
601 and electrical conductivities of the 169-nm-wide suspended GNR were about 350 W/m·K and
602 9×10^5 S/m, respectively. This thermal conductivity was about 15% of that of large-area
603 suspended graphene, which can be explained by phonon-edge scattering, but the electrical
604 conductivity was also largely reduced as compared to pristine graphene because of the
605 inevitable defects and contaminations from the lithographical processes. The ZT value of this
606 sample could be estimated to be on the order of 10^{-3} by assuming the Seebeck coefficient the
607 same as that of large-area graphene. Later, using MEMS fabricated metallic heater and sensors,
608 Hossain and co-workers [198] measured the Seebeck coefficient of graphene sheets and a
609 patterned individual 50-nm-wide GNR supported on SiO₂. The Seebeck coefficient was
610 measured to be enhanced from ~10 μ V/K for the graphene sheet to ~30 μ V/K for the GNR,
611 which demonstrated the nanostructure effect on the Seebeck coefficient although both were
612 quite low values due to the sample quality.

613 A recent work by Li *et al.* [196] finally realized the enhancement of ZT of graphene by
614 several orders of magnitude (Fig. 9 (c)). Li and co-workers [196] designed a one-process
615 approach to fabricate suspended high-quality GNRs along with an 8-terminal test device.
616 Instead of lithographical patterning, the suspended GNRs were directly synthesized by a
617 method called plasma chemical vapor deposition. In this synthesis method, a nanoscale Ni thin
618 film bridging the Ni heater and sensor acted as the catalyst and melted during the synthesis,
619 leaving the above GNR free-standing. The as-grown process ensured a low number of defects
620 and relatively smooth GNR edges, which is important for maintaining high electrical
621 conductivity. The 8-terminal device allowed simultaneous measurements of thermal and
622 electrical conductivities and the Seebeck coefficient. The 40-nm-wide and ~250-nm-long
623 samples exhibited record-high ratios of electrical conductivity to thermal conductivity for
624 graphene that were 1-2 orders of magnitude higher than those previously reported. Detailed
625 phonon BTE simulations revealed that the reduction of thermal conductivity mainly resulted
626 from quasi-ballistic phonon transport, and the significant enhancement of σ/k is attributed to
627 disparate electron and phonon MFPs and the defect-free samples. Furthermore, the Seebeck

628 coefficient was 87.7–125.7 $\mu\text{V/K}$ at 80–220 K, several times that of large-area graphene
 629 because of bandgap opening. As a result, the ZT reached record-high values for graphene of
 630 about 0.1, which demonstrated that nanostructured graphene can be a superior thermoelectric
 631 material for power generation as predicted in the theoretical studies.

632



633

634 **Fig. 9 Thermal and thermoelectric measurements of graphene nanoribbons (GNRs).**
 635 **(a) Thermal conductivity measurements of SiO₂-supported GNRs (adapted from [200]).**
 636 **(b) Thermal conductivity measurements of suspended GNRs (adapted from [197]).** (c)
 637 **Record-high ZT measured in as-grown 40-nm-wide suspended GNRs (adapted from**
 638 **[196]).**

639 **4. Van der Waals heterostructures for thermoelectrics**

640 One of the advantages of 2D materials is the ability to tune their bandgap, hence tuning
 641 the thermoelectric PF . The change in the bandgap could be achieved by changing the number
 642 of layers, applying strain or electric field, and changing the structural composition of the
 643 material (by hydrogenation or oxidation). For example, by reducing the number of layers of
 644 arsenic from its semimetallic bulk, one can observe a transition to a semiconducting state. The
 645 monolayer honeycomb structures of arsenic, called arsenide, is a semiconductor with an indirect
 646 bandgap of 0.831 eV.[201] The electronic transport of 2D layers also depends on the type of
 647 substrate used. Via long-range Coulomb interaction, the impurities in the substrate can affect
 648 the electrons moving in the 2D layer material. The lattice constant mismatch between the
 649 substrate and the 2D layer can cause strain/stress on the 2D material and modify its electronic
 650 structure. The mismatch of the crystal structure can result in breaking the symmetry and also
 651 can modify the electronic structure of the 2D layer. In the first part of this section, we focus on

652 the in-plane thermoelectric transport with the substrate and the number of layers as two
653 important parameters in mind.

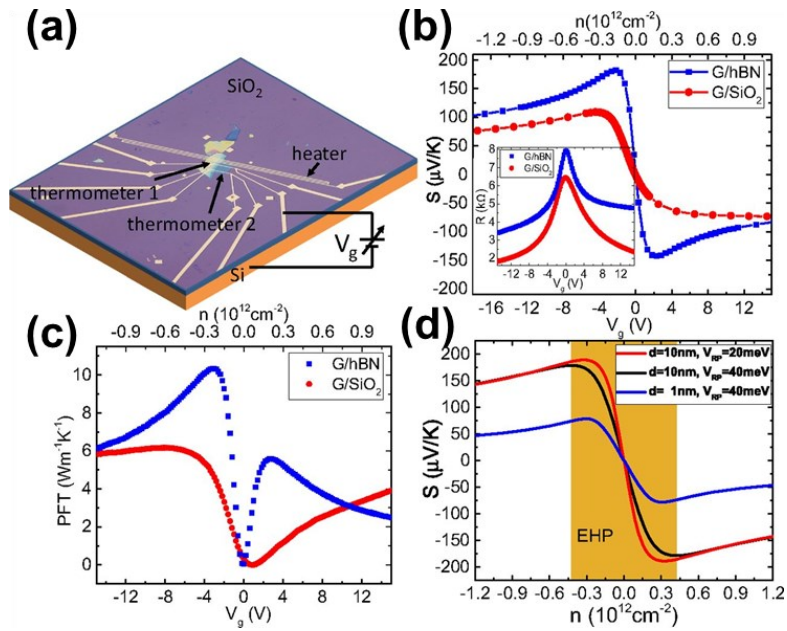
654 The discovery of 2D layered materials and the possibility of mixing and matching
655 atomically thin layers by stacking them on top of each other, open up a new exciting opportunity.
656 Millions of combination of the different 2D layers with different band structures are now
657 possible to engineer the energy potential of electronic transport, enabling the design of high-
658 PF structures. At the same time, due to the nature of the weak van der Waals bonds, these 2D
659 layered materials, inherently own very low thermal conductivity values in the cross-plane
660 direction and hence pave the way for the design of solid-state thermionic structures. In the
661 second part of this section, we focus on the cross-plane thermoelectric transport in 2D layered
662 structures with less than 10 layers.

663 4.1 In-plane transport

664 The transport properties of 2D layers are a strong function of the substrate that they are
665 placed on. In section 2, we focused on the thermoelectric properties of 2D layers placed on
666 SiO_2/Si substrate which is the most widely used substrate. Here, we summarize some of the
667 results obtained by using a different substrate or placing on hBN or graphene in between the
668 2D material and the SiO_2 substrate.

669 Duan and co-workers [5] fabricated graphene on hBN samples using the poly(methyl
670 methacrylate) (PMMA)-based dry transfer method, and patterned metallic heater and
671 thermometers on top the heterostructure for the electrical conductivity and Seebeck coefficient
672 measurements. They found that the Seebeck coefficient of graphene on hBN can be twice that
673 of graphene on SiO_2 , and measured the room-temperature PFT value of the graphene/hBN
674 device up to 10.35 W/mK (Fig. 10 (c)), which exceeded all the previously reported room-
675 temperature PFT values for both 3D and 2D materials. Duan *et al.* [5] further demonstrated that
676 the Seebeck coefficient offers a measure of the substrate-induced random potential fluctuations
677 and the hBN substrates can enable larger bipolar switching slopes for the Seebeck coefficient
678 (Fig. 10 (b) and (d)). Combining the high PF with the large thermal conductivity of both
679 graphene and boron nitride, this work by Duan and co-workers demonstrated that the
680 graphene/hBN heterostructure can be a very promising material for active cooling of electronics.
681 Wu and co-workers [213] fabricated MoS_2/hBN heterostructure samples with sulfur vacancies
682 and measured the in-plane thermoelectric properties using a similar approach as in Ref. [5]. The
683 n-type MoS_2 on hBN exhibited an extremely large positive Seebeck coefficient of 2 mV/K in
684 the on-state because of the magnetically induced Kondo effect [213]. Further, by tuning the
685 chemical potential, Wu *et al.* measured a PF as high as 50 mW/m · K² at 30K or PFT value of
686 1.5 W/mK.

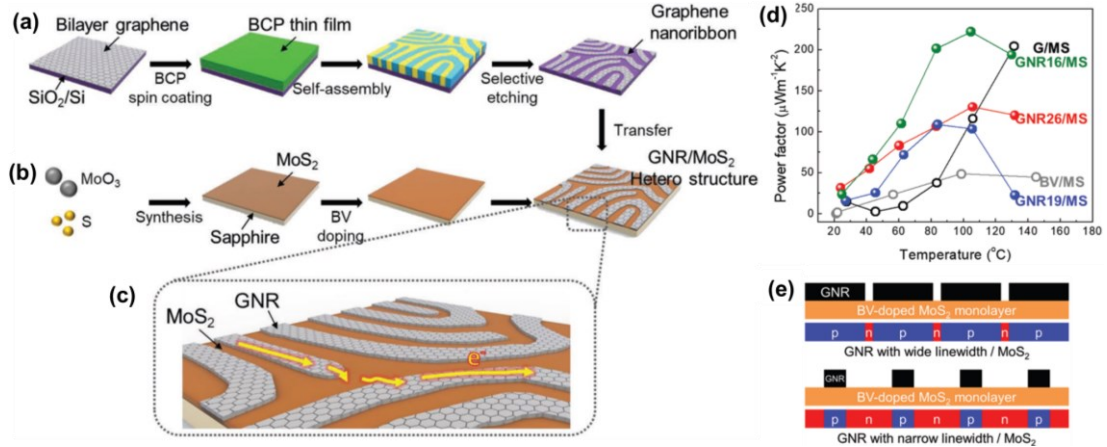
687 By combining the nanostructuring and stacking approaches, Oh and co-workers [208]
688 fabricated sub-20 nm GNR arrays on monolayer MoS_2 . They measured the in-plane electrical
689 conductivity and Seebeck coefficient of the GNR/ MoS_2 heterostructure using a commercial
690 instrument and achieved a relatively high PF of 222 $\mu\text{W}/\text{mK}^2$ [208].



691

692 **Fig. 10** A graphene/hBN heterostructure device with an enhanced in-plane *PF*. (a)
 693 Schematic of the thermoelectric measurement device. (b) Seebeck coefficients as a
 694 function of the gate voltage for G/hBN and G/SiO₂ at 290 K. (c) *PFT* as a function of the
 695 gate voltage for G/hBN and G/SiO₂ at 290 K. (d) Simulation of the Seebeck coefficient as
 696 a function of the carrier density at 300 K, with different hBN thicknesses, *d*, and random
 697 potential fluctuations, *V_{RP}*. Adapted from [5].

698



699

700 **Fig. 11** GNR/MoS₂ heterostructures with improved thermoelectric properties. (a)
 701 Fabrication of the GNR network. (b) Synthesis of doped MoS₂. (c) Schematic diagram of
 702 the in-plane carrier movement across the GNR/MoS₂ van der Waals heterojunctions. (d)
 703 The *PFs* of the GNR/MoS₂ heterostructures. (e) Schematic images of the GNR/MoS₂
 704 heterostructures with wide and narrow GNRs. Adapted from [208].

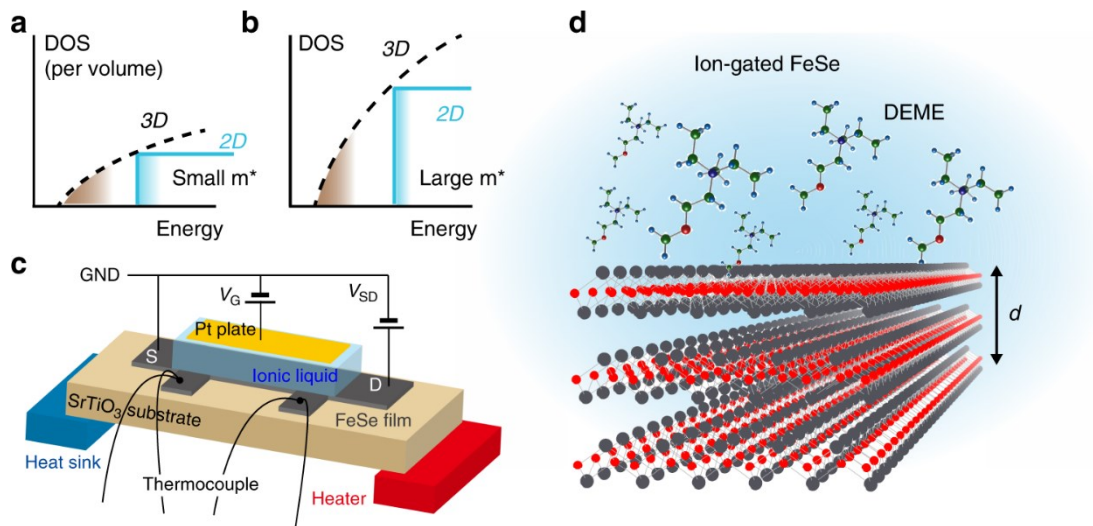
705

706 A very interesting recent work ([94], Fig. 12) shows that the thermoelectric *PF* of FeSe
 707 films, a high-*T_c* superconductor, placed on SrTiO₃ substrate increases as the thickness decreases.

708 When the films are about 1-nm thick, the equivalent of a bilayer, the thermoelectric PF
 709 increases to values as large as $1.30 \text{ W/m}\cdot\text{K}^2$ or PFT value of $390 \text{ W/m}\cdot\text{K}$. [94] This value is
 710 larger than anything reported before especially at such a low temperature. This large
 711 enhancement is attributed to the strong electronic correlation of FeSe electrons. Other
 712 possibilities such as the effect of the substrate, the ionic liquid used for gating, and the phonon
 713 drag effect are disputed by the authors but require more through theoretical insights. As
 714 mentioned in section 2, similar thickness dependence has been observed for MoS_2 placed on
 715 SiO_2 and 2L MoS_2 possesses the best PF [12],[49].

716 Other than a single graphene sample, a counterflow room-temperature PF of ~ 700
 717 $\mu\text{W}/\text{cm}\cdot\text{K}^2$ was reported for bilayer-graphene double layers separated by a thin ($\sim 20 \text{ nm}$)
 718 boron nitride layer (Fig. 13), where top and bottom gate voltages are separately applied to each
 719 graphene layer [222].

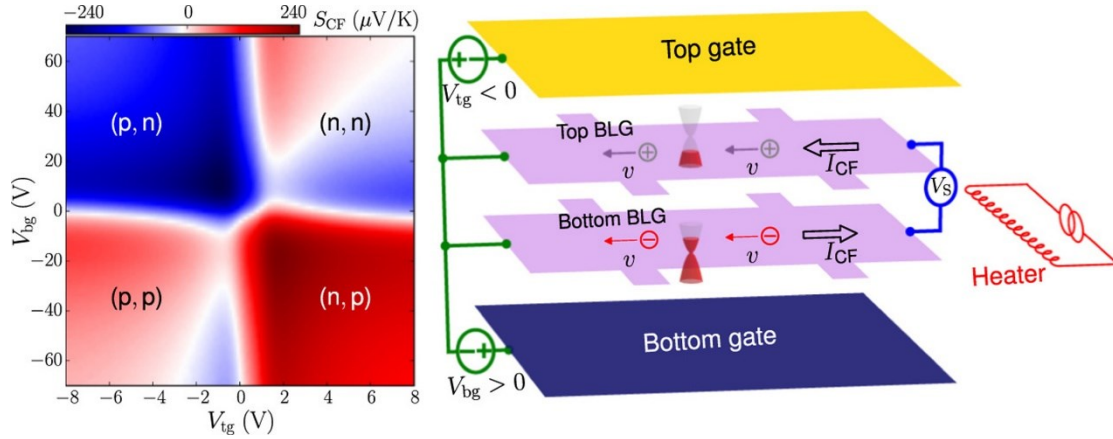
720



721

722 **Fig. 12** Thermoelectric measurement of ion-gated FeSe thin films. (a) Schematic
 723 illustration of the DOS for 3D and 2D electrons. (b) The large effective mass m^* enhances
 724 the DOS, which is beneficial for enhancing the Seebeck effect. (c) Device structure for
 725 thermoelectric measurement. (d) Enlarged illustration of the ionic liquid/FeSe interface.
 726 Adapted from [94].

727



728

729 **Fig. 13** A graphene/hBN heterostructure device with an enhanced in-plane *PF*. (a)
 730 Schematic of the thermoelectric measurement device. (b) Seebeck coefficients as a
 731 function of the gate voltage for G/hBN and G/SiO₂ at 290 K. (c) *PFT* as a function of the
 732 gate voltage for G/hBN and G/SiO₂ at 290 K. (d) Simulation of the Seebeck coefficient as
 733 a function of the carrier density at 300 K, with different hBN thicknesses, *d*, and random
 734 potential fluctuations, *V*_{RP}. Adapted from [222].

735 **4.2 Cross-plane transport: solid-state thermionic structure**

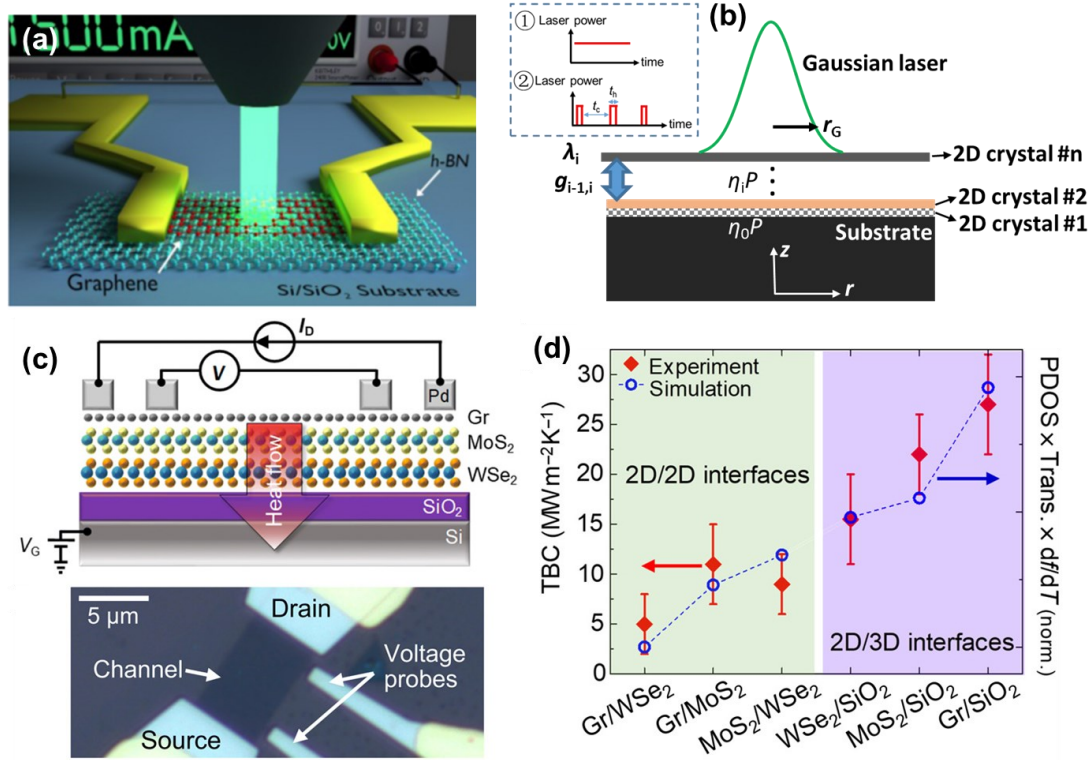
736 Here, we focus on 2D layered materials with metallic contacts on the top and the bottom
 737 and hence transport of electrons and phonons perpendicular to layer planes wherein an energy
 738 barrier is formed due to the band alignment of the heterostructure. When there is only a
 739 monolayer, transport is dominated by electron tunneling. Due to the transfer of low energy
 740 electrons, expected *ZT* values of tunneling interfaces is small. The tunneling can be eliminated
 741 by increasing the number of layers. It is shown that about 4 layers are needed to suppress the
 742 tunneling effects [223] and force the electrons to go above the energy barrier, the so-called
 743 thermionic transport is then dominant. The concept of solid-state thermionic cooling was first
 744 proposed by Shakouri [224] and later evaluated both in the power generation and the cooling
 745 mode by Mahan [225]. These structures are in between vacuum state thermionic generators and
 746 thermoelectric generators. Similar to vacuum state thermionic generators [226]–[229], there is
 747 an energy barrier that electrons need to overcome to move from the hot cathode to the cold
 748 anode. The energy barrier of a vacuum state thermionic generators is determined by the work-
 749 function of the metallic cathode and anode. Since the work function of metals is on the order
 750 of eV, temperatures larger than 1000 K are needed for electron transport. This problem is
 751 resolved in solid-state thermionic generators since the energy barrier can be adjusted to much
 752 lower values by proper choice of the metal-semiconductor interface. In these structures, the
 753 difference between the metal work function and the electron affinity of the semiconducting
 754 layer determines the electronic energy barrier. Hence by designing the energy barrier to few
 755 *k_BT*, one can design the appropriate generator for the given operating temperature, *T*. In the case
 756 of 5 to 10 layers of 2D van der Waals heterostructure, the chemical potential is pinned by the
 757 metallic contact but the energy barrier can be engineered with a high degree of flexibility by
 758 finding the right sequence of layers [230],[231].

759 When the thickness of the 2D layered material is comparable or larger than the electron
760 MFP, we see a transition from ballistic transport to diffusive transport which is closer to
761 thermoelectric transport. In this case, transport is mostly a function of the semiconducting
762 layers and the effect of the contacts is minimum and limited to the electrical and thermal contact
763 resistances at the metallic interfaces. The situation is different in solid-state thermionic
764 generators. There, due to the ballistic nature of transport, electrons are not in near equilibrium
765 with the lattice of the semiconducting layer. Hence, to understand thermionic transport, metallic
766 contacts need to be included in the analysis. The combination of cathode-semiconductor-anode
767 determines the energy barrier, the positioning of the chemical potential, and hence the
768 thermionic *PF*.

769 Several theoretical works have shown the potential of 2D van der Waals heterostructures
770 for solid-state thermionic applications and they all point to large *ZT* values. [223], [232]–[234]
771 However, all calculations are done for ideal interfaces. In practice, making such ideal clean
772 interfaces using transfer techniques is not realistic. Hence, the future of this field should be
773 guided by more experimental results.

774 In the out-of-plane direction, one of the experimental challenges is how to determine the
775 temperature gradient across the atomic thin layers for the thermal and thermoelectric
776 characterization. The Raman spectroscopy based non-contact thermometer enables
777 simultaneous temperature detection of every atomic thin material from their distinct Raman
778 peaks that shift with temperatures [34],[192],[193],[221], and thus has been employed to
779 measure the thermal boundary resistance at the van der Waals interface and the Seebeck
780 coefficient in the cross-plane direction. Chen and co-workers [207] stacked graphene on the
781 insulating hBN and patterned electrodes on graphene to provide Joule self-heating. The Joule
782 heat flux transferred across the heterojunction and the temperatures of both the graphene and
783 hBN layers were simultaneously measured from the Raman spectrum (Fig. 14 (a)), from which
784 the thermal boundary conductance (TBC) between graphene and hBN was determined to be 7.4
785 MW/m²K. Vaziri *et al.* [203] applied this technique of combining Joule heating and Raman
786 thermometry to the thermal measurement of more complicated heterostructure devices
787 involving graphene (Gr), MoS₂, and WSe₂ (Fig. 14 (c)). The TBC values at the 2D/2D interfaces
788 were measured to be 5 ± 3 MW/m²K, 10 ± 3 MW/m²K, and 9 ± 3 MW/m²K for the Gr/WSe₂,
789 Gr/MoS₂, and MoS₂/WSe₂ interfaces, respectively, which were significantly lower than those
790 at the 2D/3D(SiO₂) interfaces (Fig. 14 (d)). Besides, Li *et al.* [202] combined laser heating and
791 Raman thermometry, and developed a variable-spot-size transient Raman opto-thermal method
792 to measure both in-plane and cross-plane thermal properties of 2D heterostructures in a non-
793 contact manner (Fig. 14 (b)).

794



795

796 **Fig. 14 Raman thermometry based thermal transport measurements of 2D van der**
 797 **Waals heterostructures. (a) Measurement of TBC between graphene and hBN using the**
 798 **Joule-heating and Raman-thermometer method (adapted from [207]). (b) The variable-**
 799 **spot-size transient Raman optothermal method to measure the in-plane and cross-plane**
 800 **thermal properties of van der Waals heterostructures (adapted from [202]). (c)**
 801 **Measurement of TBC between multilayer heterostructures using the Joule-heating and**
 802 **Raman-thermometer method. (d) Measured room-temperature TBC values of 2D/2D and**
 803 **2D/3D (with SiO₂) interfaces and the calculated product of phonon DOS, phonon**
 804 **transmission, and df/dT , normalized to the minimum achieved for Gr/WSe₂. (c) and (d)**
 805 **are adapted from [203].**

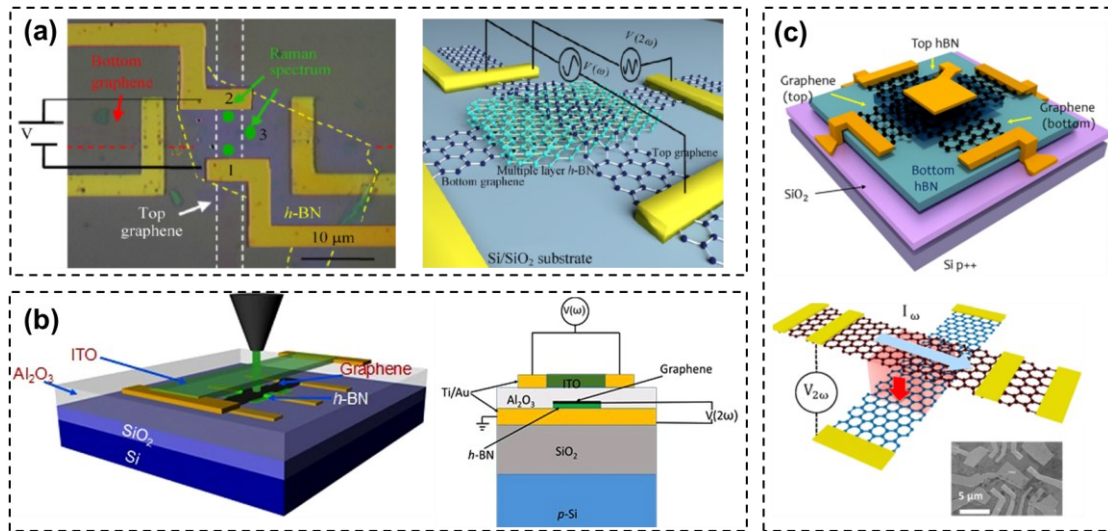
806

807 Another widely studied technique for thermal boundary resistance measurement is the
 808 time domain thermo-reflectance method (TDTR). [235] TDTR has been widely used to
 809 measure the thermal transport across various interfaces. However, only recently this method is
 810 extended to small scales enabling measurement of micron-size flakes. In the context of cross-
 811 plane thermoelectric transport measurements, TDTR is recently used to measure thermal
 812 conductance across Au/Ti (or TiOx)/WSe₂/HOPG. It is shown that the TBC depends on the
 813 details of the contact, and the level of oxidization of titanium and is in the range of 6 to 22
 814 MW/m²K. Despite the small thermal conductance values, the studied interface has a low *ZT*
 815 due to the dominance of the electronic tunneling transport. [236]

816 A few experiments have been conducted to measure the cross-plane Seebeck coefficient
 817 of 2D heterostructures. Chen *et al.* [204] stacked a Gr/hBN/Gr heterostructure as shown in Fig.
 818 15 (a), and patterned electrodes on the top and bottom graphene sheets. The top graphene was

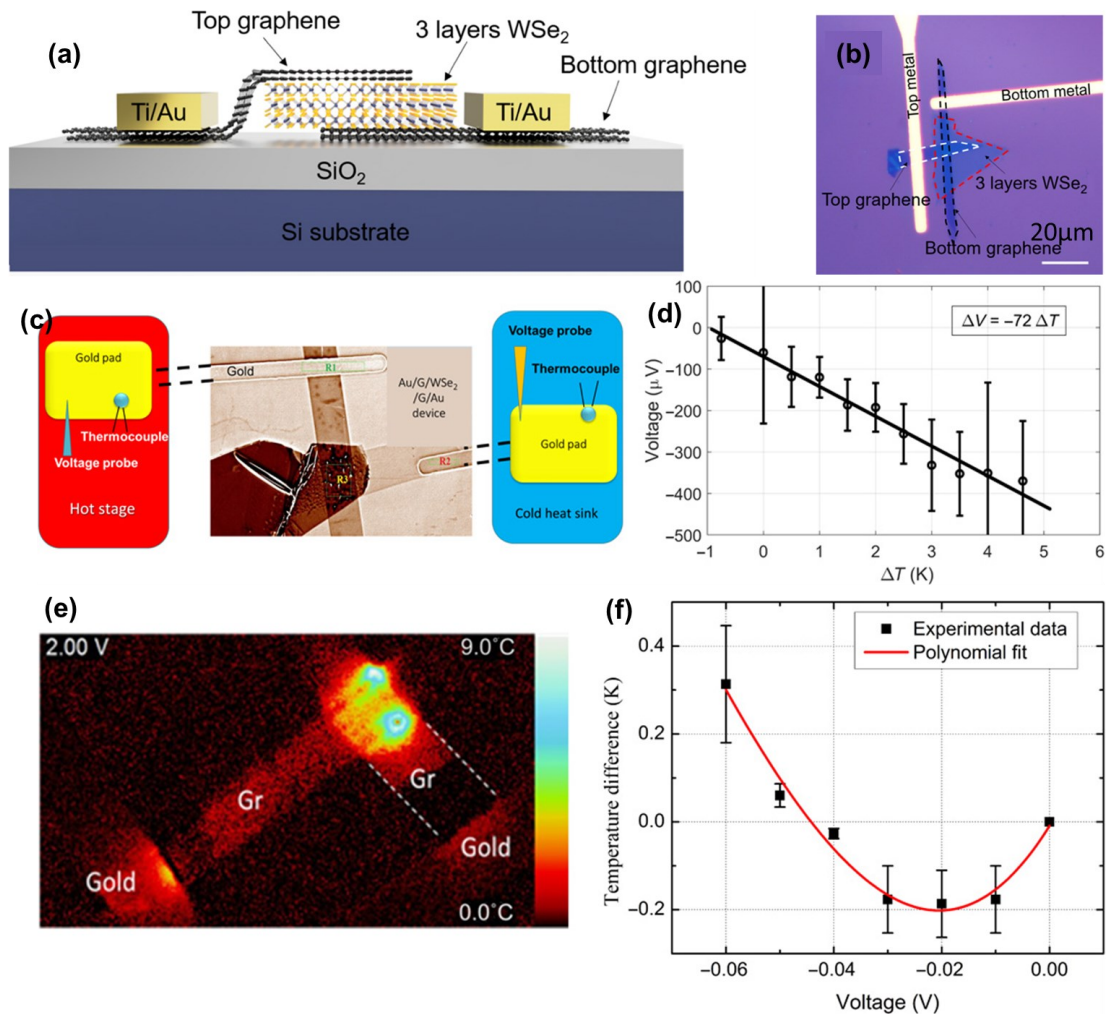
819 fed with AC current to provide Joule heating and establish a temperature gradient in the cross-
 820 plane direction. The Seebeck voltage across the top and bottom graphene was measured from
 821 the 2ω voltage using the lock-in technique, while the temperature difference was detected by
 822 the Raman thermometry. In this way, Chen *et al.* comprehensively measured the thermal
 823 conductance, Seebeck coefficient, as well as the electrical conductance in the cross-plane for
 824 the same heterostructure device. The cross-plane Seebeck coefficient was $-99.3 \mu\text{V/K}$, the PF
 825 (S^2G) was $1.51 \times 10^{-15} \text{ W/K}^2$, and the ZT was 1.05×10^{-6} for the Gr/hBN/Gr heterostructure. The
 826 extremely low ZT is the result of the low electrical conductance which in turn is due to the large
 827 energy barrier formed by the insulating hBN layer. Poudel and co-workers [206] reported a
 828 modified test device where the insulating Al_2O_3 and an indium tin oxide (ITO) transparent
 829 heater were coated on the Gr/hBN/Au heterostructure (Fig. 15 (b)). Similar with the work by
 830 Chen *et al.*, while the transparent top heater was driven with AC current to provide heat flux in
 831 the cross-plane direction, the temperature difference between graphene and hBN was measured
 832 from their Raman peaks and the cross-plane Seebeck coefficient was detected from the lock-in
 833 2ω voltage, which yielded an interfacial Seebeck coefficient of $-215 \mu\text{V/K}$. Mahapatra and co-
 834 workers [205] stacked two layers of graphene sheets encapsulated by hBN using the layer-by-
 835 layer mechanical transfer method, as illustrated in Fig. 15 (c). The top graphene was conducted
 836 with AC current and the Seebeck coefficient across the twisted bilayer graphene was measured
 837 by the lock-in technique, while the temperatures of the two monolayers were determined from
 838 the temperature dependence of the in-plane electrical resistance of each graphene sheet. The
 839 maximum Seebeck coefficient of the van der Waals junction between graphene layers was
 840 measured to be $20\text{--}25 \mu\text{V/K}$ at a carrier density of $1 \times 10^{11} \text{ cm}^{-2}$ at $\sim 70 \text{ K}$.

841



842

843 **Fig. 15** Cross-plane Seebeck coefficient measurements of 2D van der Waals
 844 heterostructures. (a) Measurement of cross-plane Seebeck coefficient of a
 845 graphene/hBN/graphene heterostructure using Raman thermometry (adapted from
 846 [204]). (b) Measurement of cross-plane Seebeck coefficient of graphene/hBN/Au
 847 heterostructures using Raman thermometry (adapted from [206]). (c) Measurement of
 848 Seebeck coefficient across the van der Waals junction in bilayer graphene (adapted from
 849 [205]).



851

852 **Fig. 16 Thermionic transport measurement across gold/Gr/WSe₂ van der Waals**
 853 **heterostructures. (a) Illustration of the cross-section of the Au/Gr/WSe₂/Gr/Au**
 854 **structure. (b) Optical microscope image of an Au/Gr/WSe₂/Gr/Au device. (c) Schematic**
 855 **of the Seebeck measurement setup. (d) Seebeck voltage measured versus applied**
 856 **temperature difference. (e) Joule heating: 2D temperature map of the Au/Gr/WSe₂/Gr/Au**
 857 **device under a relatively high-voltage 2 V obtained using the thermoreflectance method.**
 858 **(f) Cooling curve: Temperature difference between the substrate and top of the active**
 859 **device in Kelvin versus applied voltage at small applied voltages. Adapted from [237].**

860

861 Rosul *et al.* [237] used a combination of TDTR measurements for determining the thermal
 862 conductance, the thermo-reflectance method for cooling curve measurements, and direct
 863 Seebeck measurement using thermocouples to study Au/Gr/WSe₂/Gr/Au structures (Fig. 16).
 864 They estimated a ZT value of 10^{-3} at RT which is the largest reported for nanometer-size
 865 thermionic structures. This small ZT is close to the predicted ZT using first-principles
 866 calculations and at RT for this structure. Theoretically, it is predicted that the ZT can be
 867 significantly improved by increasing the operating temperature and by changing the electrodes

868 from gold to platinum with a lower formed energy barrier. Hence developing the transport
869 measurement techniques enabling high-temperature measurements, and developing techniques
870 for more flexible fabrication of a variety of different metals-2D layers with clean interfaces,
871 seems to be the most immediate need for further development of the 2D van der Waals based
872 thermionic generators.

873 **5. Summary and outlook**

874 Instead of search for new materials, existing 2D materials can be tailored for their transport,
875 optical, magnetic and other properties simply by patterned nanostructures and stacked forms.
876 Tremendous research opportunities exist in device- and energy-related applications. However,
877 there is still many important issues to be addressed. First, accurate thermoelectric measurements
878 for such fragile samples are still challenging and caution should be taken for the
879 electrical/thermal contacts to the samples. For ZT calculations, the same sample must be
880 measured along the same direction for all three thermoelectric properties. This can be more
881 difficult in some cases and an integrated measurement setup is required to simultaneously
882 measure all properties, as demonstrated for nanoporous Si thin films [238]. Second, theoretical
883 calculations often suggested the impact of detailed atomic structures, e.g., structure disorder,
884 chirality, zigzag or armchair edges. This has been largely neglected in measurements. A unified
885 picture is still missing here. In addition, the disconnection between theoretical studies and
886 experimental measurements can also be found in the structure dimension, where ultrafine
887 nanoporous 2D materials are still hard to be fabricated. In this aspect, directly grown 2D porous
888 materials with uniform sub-1 nm holes [239],[240] may allow direct comparison between
889 theoretical and experimental studies. High-energy electron or ion beam can also be used to drill
890 sub-1 nm pores but attention should be paid to the atomic structure around pores [241]–[243].
891 Third, more advancements are required in first-principles predictions of the transport properties.
892 For materials genome, a high-throughput calculation method is required and this can be
893 achieved with machine learning. Successful examples for machine learning in materials search
894 and design can be found for interfacial thermal conductance [165],[244],[245], bandgap [246],
895 and interatomic force constants [247],[248],[249] used in MD simulations. Machine learning
896 driven by experimental data is desired for thermoelectric studies, but is still lacking due to the
897 challenge of high-throughput measurements at the nanoscale. Finally, the device-level
898 applications of these materials and their mass production should receive more attention. The
899 high nanofabrication cost of some nanostructured or stacked 2D materials may hinder their
900 wide applications.

901 **Acknowledgments**

902 This work was partially supported by JSPS KAKENHI (Grant No. JP20H02090) and the
903 JST CREST Grant Number JPMJCR18I1, Japan. Hao acknowledges the support from NSF
904 (grant number CBET-1803931). Zebarjadi acknowledges the support from NSF grant number
905 1653268.

906 **References**

- 907 [1] Dollfus, P., Nguyen, V. H., & Saint-Martin, J. (2015). Thermoelectric effects in graphene
908 nanostructures. *Journal of Physics: Condensed Matter*, 27(13), 133204.
- 909 [2] Markov, M., & Zebarjadi, M. (2019). Thermoelectric transport in graphene and 2D layered
910 materials. *Nanoscale and Microscale Thermophysical Engineering*, 23(2), 117-127.
- 911 [3] M. Zebarjadi, Electronic cooling using thermoelectric devices, *Appl. Phys. Lett.* 106
912 (2015) 203506. <https://doi.org/10.1063/1.4921457>.
- 913 [4] M.J. Adams, M. Verosky, M. Zebarjadi, J.P. Heremans, Active Peltier Coolers Based on
914 Correlated and Magnon-Drag Metals, *Phys. Rev. Appl.* 11 (2019) 054008.
915 <https://doi.org/10.1103/PhysRevApplied.11.054008>.
- 916 [5] J. Duan, X. Wang, X. Lai, G. Li, K. Watanabe, T. Taniguchi, M. Zebarjadi, E.Y. Andrei,
917 High thermoelectric power factor in graphene/hBN devices, *Proc. Natl. Acad. Sci.* 113
918 (2016) 14272–14276. <https://doi.org/10.1073/pnas.1615913113>.
- 919 [6] Lundstrom, M. S., & Jeong, C. (2012). *Near-Equilibrium Transport: Fundamentals and*
920 *Applications (Vol. 2)*. World Scientific Publishing Company.
- 921 [7] Jeong, C., Kim, R., Luisier, M., Datta, S., & Lundstrom, M. (2010). On Landauer versus
922 Boltzmann and full band versus effective mass evaluation of thermoelectric transport
923 coefficients. *Journal of Applied Physics*, 107(2), 023707.
- 924 [8] Fisher, Timothy S. *Thermal energy at the nanoscale*. Vol. 3. World Scientific Publishing
925 Company, 2013.
- 926 [9] Mahan, G. D.; Sofo, J. O. The best thermoelectric. *Proceedings of the National Academy*
927 *of Sciences*, 1996, 93.15: 7436-7439.
- 928 [10] Seol, J. H., Jo, I., Moore, A. L., Lindsay, L., Aitken, Z. H., Pettes, M. T., ... & Mingo, N.
929 (2010). Two-dimensional phonon transport in supported graphene. *Science*, 328(5975),
930 213-216.
- 931 [11] Y.M. Zuev, W. Chang, P. Kim, Thermoelectric and Magnetothermoelectric Transport
932 Measurements of Graphene, *Phys. Rev. Lett.* 102 (2009) 096807.
933 <https://doi.org/10.1103/PhysRevLett.102.096807>.
- 934 [12] Hippalgaonkar, K., Wang, Y., Ye, Y., Qiu, D. Y., Zhu, H., Wang, Y., ... & Zhang, X.
935 (2017). High thermoelectric power factor in two-dimensional crystals of MoS₂. *Physical*
936 *Review B*, 95(11), 115407.
- 937 [13] Hicks, L. D., and Dresselhaus, M. S. "Effect of quantum-well structures on the
938 thermoelectric figure of merit." *Physical Review B* 47.19 (1993): 12727.
- 939 [14] Hicks, L. D., and Dresselhaus, M. S. "Thermoelectric figure of merit of a one-dimensional
940 conductor." *Physical review B* 47.24 (1993): 16631.

- 941 [15] Mao, J., Liu, Z., & Ren, Z. (2016). Size effect in thermoelectric materials. *npj Quantum*
942 *Materials*, 1(1), 1-9.
- 943 [16] Xiao, Y., Chen, Q., Ma, D., Yang, N., & Hao, Q. (2019). Phonon Transport within Periodic
944 Porous Structures--From Classical Phonon Size Effects to Wave Effects. *ES Materials &*
945 *Manufacturing*, 5, 2-18.
- 946 [17] Novoselov, K. S., Mishchenko, A., Carvalho, A., & Neto, A. C. (2016). 2D materials and
947 van der Waals heterostructures. *Science*, 353(6298), aac9439.
- 948 [18] Geim, A. K., & Grigorieva, I. V. (2013). Van der Waals heterostructures. *Nature*,
949 499(7459), 419-425.
- 950 [19] Mounet, N., Gibertini, M., Schwaller, P., Campi, D., Merkys, A., Marrazzo, A., ... &
951 Marzari, N. (2018). Two-dimensional materials from high-throughput computational
952 exfoliation of experimentally known compounds. *Nature nanotechnology*, 13(3), 246-252.
- 953 [20] Xu, Y., Li, Z., & Duan, W. (2014). Thermal and thermoelectric properties of
954 graphene. *Small*, 10(11), 2182-2199.
- 955 [21] Zhang, G., & Zhang, Y. W. (2017). Thermoelectric properties of two-dimensional
956 transition metal dichalcogenides. *Journal of Materials Chemistry C*, 5(31), 7684-7698.
- 957 [22] Jing Wu, Yabin Chen, Junqiao Wu, Kedar Hippalgaonkar. Perspectives on
958 Thermoelectricity in Layered and 2D Materials. *Advanced Electronic Materials* 2018, 4
959 (12), 1800248. DOI: 10.1002/aelm.201800248.
- 960 [23] Zhao, Y., Cai, Y., Zhang, L., Li, B., Zhang, G., & Thong, J. T. (2019). Thermal Transport
961 in 2D Semiconductors—Considerations for Device Applications. *Advanced Functional*
962 *Materials*, 1903929.
- 963 [24] Kanahashi, Kaito; Pu, Jiang; Takenobu, Taishi. 2D Materials for Large-Area Flexible
964 Thermoelectric Devices. *Advanced Energy Materials*, 2019, 1902842.
- 965 [25] Zong, P. A., Liang, J., Zhang, P., Wan, C., Wang, Y., & Koumoto, K. (2020). Graphene-
966 Based Thermoelectrics. *ACS Applied Energy Materials*, 3(3), 2224-2239.
- 967 [26] Li, D., Gong, Y., Chen, Y., Lin, J., Khan, Q., Zhang, Y., ... & Xie, H. (2020). Recent
968 Progress of Two-Dimensional Thermoelectric Materials. *Nano-Micro Letters*, 12(1), 36.
- 969 [27] Sankeshwar, N. S., Kubakaddi, S. S., & Mulimani, B. G. (2013). Thermoelectric power in
970 graphene. *Advances in Graphene Science*, 10, 56720.
- 971 [28] Wei P, Bao W, Pu Y, Lau C and Shi J 2009 Anomalous thermoelectric transport of dirac
972 particles in graphene *Phys. Rev. Lett.* 102 166808
- 973 [29] Checkelsky J and Ong N 2009 Thermopower and Nernst effect in graphene in a magnetic
974 field *Phys. Rev. B* 80 081413

- 975 [30] Wu X, Hu Y, Ruan M, Madiomanana N K, Berger C and de Heer W A 2011
976 Thermoelectric effect in high mobility single layer epitaxial graphene Appl. Phys. Lett. 99
977 133102
- 978 [31] Sadeghi, M. M., Jo, I., & Shi, L. (2013). Phonon-interface scattering in multilayer
979 graphene on an amorphous support. Proceedings of the National Academy of
980 Sciences, 110(41), 16321-16326.
- 981 [32] Pop, E., Varshney, V., & Roy, A. K. (2012). Thermal properties of graphene:
982 Fundamentals and applications. MRS bulletin, 37(12), 1273-1281.
- 983 [33] Balandin, A. A. (2011). Thermal properties of graphene and nanostructured carbon
984 materials. Nature materials, 10(8), 569-581.
- 985 [34] Li, Q. Y., Xia, K., Zhang, J., Zhang, Y., Li, Q., Takahashi, K., & Zhang, X. (2017).
986 Measurement of specific heat and thermal conductivity of supported and suspended
987 graphene by a comprehensive Raman optothermal method. Nanoscale, 9(30), 10784-
988 10793.
- 989 [35] Gu, X., Fan, Z., Bao, H., & Zhao, C. Y. (2019). Revisiting phonon-phonon scattering in
990 single-layer graphene. Physical Review B, 100(6), 064306.
- 991 [36] Zhang, Y., Tang, T. T., Girit, C., Hao, Z., Martin, M. C., Zettl, A., ... & Wang, F. (2009).
992 Direct observation of a widely tunable bandgap in bilayer graphene. Nature, 459(7248),
993 820-823.
- 994 [37] Lui, C. H., Li, Z., Mak, K. F., Cappelluti, E., & Heinz, T. F. (2011). Observation of an
995 electrically tunable band gap in trilayer graphene. Nature Physics, 7(12), 944-947.
- 996 [38] Bao, W., Jing, L., Velasco, J., Lee, Y., Liu, G., Tran, D., ... & Koshino, M. (2011).
997 Stacking-dependent band gap and quantum transport in trilayer graphene. Nature
998 Physics, 7(12), 948-952.
- 999 [39] Cao, Y., Fatemi, V., Fang, S., Watanabe, K., Taniguchi, T., Kaxiras, E., & Jarillo-Herrero,
1000 P. (2018). Unconventional superconductivity in magic-angle graphene
1001 superlattices. Nature, 556(7699), 43-50.
- 1002 [40] Nam S-G, Ki D-K and Lee H-J 2010 Thermoelectric transport of massive Dirac fermions
1003 in bilayer graphene Phys. Rev. B 82 245416
- 1004 [41] Wang, C. R., Lu, W. S., Hao, L., Lee, W. L., Lee, T. K., Lin, F., ... & Chen, J. Z. (2011).
1005 Enhanced thermoelectric power in dual-gated bilayer graphene. Physical review
1006 letters, 107(18), 186602.
- 1007 [42] Chien, Y. Y., Yuan, H., Wang, C. R., & Lee, W. L. (2016). Thermoelectric power in
1008 bilayer graphene device with ionic liquid gating. Scientific reports, 6, 20402.
- 1009 [43] Suszalski, D., Rut, G., & Rycerz, A. (2019). Thermoelectric properties of gapped bilayer
1010 graphene. Journal of Physics: Condensed Matter, 31(41), 415501.

- 1011 [44] Manzeli, S., Ovchinnikov, D., Pasquier, D., Yazyev, O. V., & Kis, A. (2017). 2D transition
1012 metal dichalcogenides. *Nature Reviews Materials*, 2(8), 17033.
- 1013 [45] Huang, W., Da, H., & Liang, G. (2013). Thermoelectric performance of MX_2 (M= Mo, W;
1014 X= S, Se) monolayers. *Journal of Applied Physics*, 113(10), 104304.
- 1015 [46] Wickramaratne, D., Zahid, F., & Lake, R. K. (2014). Electronic and thermoelectric
1016 properties of few-layer transition metal dichalcogenides. *The Journal of chemical physics*,
1017 140(12), 124710.
- 1018 [47] Huang, W., Luo, X., Gan, C. K., Quek, S. Y., & Liang, G. (2014). Theoretical study of
1019 thermoelectric properties of few-layer MoS_2 and WSe_2 . *Physical Chemistry Chemical*
1020 *Physics*, 16(22), 10866-10874.
- 1021 [48] Wu, J., Schmidt, H., Amara, K. K., Xu, X., Eda, G., & Özyilmaz, B. (2014). Large
1022 thermoelectricity via variable range hopping in chemical vapor deposition grown single-
1023 layer MoS_2 . *Nano Letters*, 14(5), 2730-2734.
- 1024 [49] M. Kayyalha, J. Maassen, M. Lundstrom, L. Shi, Y.P. Chen, Gate-tunable and thickness-
1025 dependent electronic and thermoelectric transport in few-layer MoS_2 , *J. Appl. Phys.* 120
1026 (2016) 134305. <https://doi.org/10.1063/1.4963364>.
- 1027 [50] Jin, Z., Liao, Q., Fang, H., Liu, Z., Liu, W., Ding, Z., ... & Yang, N. (2015). A revisit to
1028 high thermoelectric performance of single-layer MoS_2 . *Scientific reports*, 5, 18342.
- 1029 [51] Li, Z., Lv, Y., Ren, L., Li, J., Kong, L., Zeng, Y., ... & Wang, D. (2020). Efficient strain
1030 modulation of 2D materials via polymer encapsulation. *Nature communications*, 11(1), 1-
1031 8.
- 1032 [52] Yoshida, M., Iizuka, T., Saito, Y., Onga, M., Suzuki, R., Zhang, Y., ... & Shimizu, S.
1033 (2016). Gate-optimized thermoelectric power factor in ultrathin WSe_2 single crystals.
1034 *Nano Letters*, 16(3), 2061-2065.
- 1035 [53] Liu, J., Choi, G. M., & Cahill, D. G. (2014). Measurement of the anisotropic thermal
1036 conductivity of molybdenum disulfide by the time-resolved magneto-optic Kerr
1037 effect. *Journal of Applied Physics*, 116(23), 233107.
- 1038 [54] Jiang, P., Qian, X., Gu, X., & Yang, R. (2017). Probing Anisotropic Thermal Conductivity
1039 of Transition Metal Dichalcogenides MX_2 (M= Mo, W and X= S, Se) using Time -
1040 Domain Thermoreflectance. *Advanced Materials*, 29(36), 1701068.
- 1041 [55] Chiritescu, C., Cahill, D. G., Nguyen, N., Johnson, D., Bodapati, A., Keblinski, P., &
1042 Zschack, P. (2007). Ultralow thermal conductivity in disordered, layered WSe_2 crystals.
1043 *Science*, 315(5810), 351-353.
- 1044 [56] Lindroth, D. O., & Erhart, P. (2016). Thermal transport in van der Waals solids from first-
1045 principles calculations. *Physical Review B*, 94(11), 115205.

- 1046 [57] Yan, R., Simpson, J. R., Bertolazzi, S., Brivio, J., Watson, M., Wu, X., ... & Xing, H. G.
1047 (2014). Thermal conductivity of monolayer molybdenum disulfide obtained from
1048 temperature-dependent Raman spectroscopy. *ACS Nano*, 8(1), 986-993.
- 1049 [58] Yu, Y., Minhaj, T., Huang, L., Yu, Y., & Cao, L. (2020). In-Plane and Interfacial Thermal
1050 Conduction of Two-Dimensional Transition-Metal Dichalcogenides. *Physical Review
1051 Applied*, 13(3), 034059.
- 1052 [59] Yuan, P., Wang, R., Wang, T., Wang, X., & Xie, Y. (2018). Nonmonotonic thickness-
1053 dependence of in-plane thermal conductivity of few-layered MoS₂: 2.4 to 37.8
1054 nm. *Physical Chemistry Chemical Physics*, 20(40), 25752-25761.
- 1055 [60] Yuan, P., Wang, R., Tan, H., Wang, T., & Wang, X. (2017). Energy Transport State
1056 Resolved Raman for Probing Interface Energy Transport and Hot Carrier Diffusion in
1057 Few-Layered MoS₂. *ACS Photonics*, 4(12), 3115-3129.
- 1058 [61] Wang, R., Wang, T., Zobeiri, H., Yuan, P., Deng, C., Yue, Y., ... & Wang, X. (2018).
1059 Measurement of the thermal conductivities of suspended MoS₂ and MoSe₂ by nanosecond
1060 ET-Raman without temperature calibration and laser absorption
1061 evaluation. *Nanoscale*, 10(48), 23087-23102.
- 1062 [62] Wang, R., Zobeiri, H., Xie, Y., Wang, X., Zhang, X., & Yue, Y. (2020) Distinguishing
1063 Optical and Acoustic Phonon Temperatures and Their Energy Coupling Factor under
1064 Photon Excitation in nm 2D Materials. *Advanced Science*, 2000097.
- 1065 [63] N. Peimyoo, J. Shang, W. Yang, Y. Wang, C. Cong, and T. Yu, Thermal conductivity
1066 determination of suspended mono-and bilayer WS₂ by Raman spectroscopy, *Nano Res.* 8,
1067 1210 (2015).
- 1068 [64] Jo, I., Pettes, M. T., Ou, E., Wu, W., & Shi, L. (2014). Basal-plane thermal conductivity
1069 of few-layer molybdenum disulfide. *Applied Physics Letters*, 104(20), 201902.
- 1070 [65] Yarali, M., Wu, X., Gupta, T., Ghoshal, D., Xie, L., Zhu, Z., ... & Koratkar, N. (2017).
1071 Effects of Defects on the Temperature - Dependent Thermal Conductivity of Suspended
1072 Monolayer Molybdenum Disulfide Grown by Chemical Vapor Deposition. *Advanced
1073 Functional Materials*, 27(46), 1704357.
- 1074 [66] Aiyiti, A., Bai, X., Wu, J., Xu, X., & Li, B. (2018). Measuring the thermal conductivity
1075 and interfacial thermal resistance of suspended MoS₂ using electron beam self-heating
1076 technique. *Science Bulletin*, 63(7), 452-458.
- 1077 [67] Gu, X., & Yang, R. (2014). Phonon transport in single-layer transition metal
1078 dichalcogenides: A first-principles study. *Applied Physics Letters*, 105(13), 131903.
- 1079 [68] Xu, K., Gabourie, A. J., Hashemi, A., Fan, Z., Wei, N., Farimani, A. B., ... & Ala-Nissila,
1080 T. (2019). Thermal transport in MoS₂ from molecular dynamics using different empirical
1081 potentials. *Physical Review B*, 99(5), 054303.
- 1082 [69] Gu, X., Li, B., & Yang, R. (2016). Layer thickness-dependent phonon properties and
1083 thermal conductivity of MoS₂. *Journal of Applied Physics*, 119(8), 085106.

- 1084 [70] Zhou, W. X., & Chen, K. Q. (2015). First-principles determination of ultralow thermal
1085 conductivity of monolayer WSe₂. *Scientific reports*, 5, 15070.
- 1086 [71] Wan, C., Gu, X., Dang, F., Itoh, T., Wang, Y., Sasaki, H., ... & Yang, R. (2015). Flexible
1087 n-type thermoelectric materials by organic intercalation of layered transition metal
1088 dichalcogenide TiS₂. *Nature Materials*, 14(6), 622-627.
- 1089 [72] Li, L., Yu, Y., Ye, G. J., Ge, Q., Ou, X., Wu, H., ... & Zhang, Y. (2014). Black phosphorus
1090 field-effect transistors. *Nature nanotechnology*, 9(5), 372.
- 1091 [73] Luo, Z., Maassen, J., Deng, Y., Du, Y., Garrelts, R. P., Lundstrom, M. S., ... & Xu, X.
1092 (2015). Anisotropic in-plane thermal conductivity observed in few-layer black phosphorus.
1093 *Nature communications*, 6(1), 1-8.
- 1094 [74] Jang, H., Wood, J. D., Ryder, C. R., Hersam, M. C., & Cahill, D. G. (2015). Anisotropic
1095 thermal conductivity of exfoliated black phosphorus. *Advanced Materials*, 27(48), 8017-
1096 8022.
- 1097 [75] Lee, S., Yang, F., Suh, J., Yang, S., Lee, Y., Li, G., ... & Park, J. (2015). Anisotropic in-
1098 plane thermal conductivity of black phosphorus nanoribbons at temperatures higher than
1099 100 K. *Nature communications*, 6(1), 1-7.
- 1100 [76] Smith, B., Vermeersch, B., Carrete, J., Ou, E., Kim, J., Mingo, N., ... & Shi, L. (2017).
1101 Temperature and thickness dependences of the anisotropic in-plane thermal conductivity
1102 of black phosphorus. *Advanced Materials*, 29(5), 1603756.
- 1103 [77] Lv, H.Y., Lu, W.J., Shao, D.F. and Sun, Y.P., 2014. Enhanced thermoelectric performance
1104 of phosphorene by strain-induced band convergence. *Physical Review B*, 90(8), p.085433.
- 1105 [78] Qin, G., Yan, Q. B., Qin, Z., Yue, S. Y., Cui, H. J., Zheng, Q. R., & Su, G. (2014). Hinge-
1106 like structure induced unusual properties of black phosphorus and new strategies to
1107 improve the thermoelectric performance. *Scientific reports*, 4, 6946.
- 1108 [79] Flores, E., Ares, J. R., Castellanos-Gomez, A., Barawi, M., Ferrer, I. J., & Sánchez, C.
1109 (2015). Thermoelectric power of bulk black-phosphorus. *Applied Physics Letters*, 106(2),
1110 022102.
- 1111 [80] Saito, Y., Iizuka, T., Koretsune, T., Arita, R., Shimizu, S., & Iwasa, Y. (2016). Gate-tuned
1112 thermoelectric power in black phosphorus. *Nano letters*, 16(8), 4819-4824.
- 1113 [81] Fei, R., Faghaninia, A., Soklaski, R., Yan, J. A., Lo, C., & Yang, L. (2014). Enhanced
1114 thermoelectric efficiency via orthogonal electrical and thermal conductances in
1115 phosphorene. *Nano letters*, 14(11), 6393-6399.
- 1116 [82] Choi, S. J., Kim, B. K., Lee, T. H., Kim, Y. H., Li, Z., Pop, E., ... & Bae, M. H. (2016).
1117 Electrical and thermoelectric transport by variable range hopping in thin black phosphorus
1118 devices. *Nano letters*, 16(7), 3969-3975.
- 1119 [83] Zare, M., Rameshti, B. Z., Ghamsari, F. G., & Asgari, R. (2017). Thermoelectric transport
1120 in monolayer phosphorene. *Physical Review B*, 95(4), 045422.

- 1121 [84] Zhao, L. D., Lo, S. H., Zhang, Y., Sun, H., Tan, G., Uher, C., ... & Kanatzidis, M. G.
1122 (2014). Ultralow thermal conductivity and high thermoelectric figure of merit in SnSe
1123 crystals. *Nature*, 508(7496), 373-377.
- 1124 [85] Heo, S. H., Jo, S., Kim, H. S., Choi, G., Song, J. Y., Kang, J. Y., ... & Jung, J. (2019).
1125 Composition change-driven texturing and doping in solution-processed SnSe
1126 thermoelectric thin films. *Nature communications*, 10(1), 1-10.
- 1127 [86] Shi, X. L., Tao, X., Zou, J., & Chen, Z. G. (2020). High - Performance Thermoelectric
1128 SnSe: Aqueous Synthesis, Innovations, and Challenges. *Advanced Science*, 7(7), 1902923.
- 1129 [87] Zhao, L. D., Chang, C., Tan, G., & Kanatzidis, M. G. (2016). SnSe: a remarkable new
1130 thermoelectric material. *Energy & Environmental Science*, 9(10), 3044-3060.
- 1131 [88] Zhou, Y., & Zhao, L. D. (2017). Promising thermoelectric bulk materials with 2D
1132 structures. *Advanced Materials*, 29(45), 1702676.
- 1133 [89] Lin, S., Li, W., Chen, Z., Shen, J., Ge, B., & Pei, Y. (2016). Tellurium as a high-
1134 performance elemental thermoelectric. *Nature communications*, 7(1), 1-6.
- 1135 [90] Sharma, S., Singh, N., & Schwingenschlögl, U. (2018). Two-dimensional tellurene as
1136 excellent thermoelectric material. *ACS Applied Energy Materials*, 1(5), 1950-1954.
- 1137 [91] Gao, Z., Liu, G., & Ren, J. (2018). High thermoelectric performance in two-dimensional
1138 tellurium: An ab initio study. *ACS applied materials & interfaces*, 10(47), 40702-40709.
- 1139 [92] Qiu, G., Huang, S., Segovia, M., Venuthurumilli, P. K., Wang, Y., Wu, W., ... & Ye, P. D.
1140 (2019). Thermoelectric performance of 2D tellurium with accumulation contacts. *Nano*
1141 *letters*, 19(3), 1955-1962.
- 1142 [93] Zhang, X., Liu, C., Tao, Y., Li, Y., Guo, Y., Chen, Y., ... & Wang, J. (2020). High ZT 2D
1143 Thermoelectrics by Design: Strong Interlayer Vibration and Complete Band - Extrema
1144 Alignment. *Advanced Functional Materials*.
- 1145 [94] S. Shimizu, J. Shiogai, N. Takemori, S. Sakai, H. Ikeda, R. Arita, T. Nojima, A. Tsukazaki,
1146 Y. Iwasa, Giant thermoelectric power factor in ultrathin FeSe superconductor, *Nat.*
1147 *Commun.* 10 (2019). <https://doi.org/10.1038/s41467-019-08784-z>.
- 1148 [95] Lee, M. J., Ahn, J. H., Sung, J. H., Heo, H., Jeon, S. G., Lee, W., ... & Jo, M. H. (2016).
1149 Thermoelectric materials by using two-dimensional materials with negative correlation
1150 between electrical and thermal conductivity. *Nature Communications*, 7(1), 1-7.
- 1151 [96] Shimizu, S., Bahramy, M. S., Iizuka, T., Ono, S., Miwa, K., Tokura, Y., & Iwasa, Y. (2016).
1152 Enhanced thermopower in ZnO two-dimensional electron gas. *Proceedings of the National*
1153 *Academy of Sciences*, 113(23), 6438-6443.
- 1154 [97] Hung, N. T., Nugraha, A. R., & Saito, R. (2017). Two-dimensional InSe as a potential
1155 thermoelectric material. *Applied Physics Letters*, 111(9), 092107.

- 1156 [98] Sharma, S., Kumar, S., & Schwingenschlögl, U. (2017). Arsenene and antimonene: two-
1157 dimensional materials with high thermoelectric figures of merit. *Physical Review Applied*,
1158 8(4), 044013.
- 1159 [99] Yu, J., Li, T., & Sun, Q. (2019). Single-layer BiOBr: An effective p-type 2D thermoelectric
1160 material. *Journal of Applied Physics*, 125(20), 205111.
- 1161 [100] Esfarjani, K., Chen, G., & Stokes, H. T. (2011). Heat transport in silicon from first-
1162 principles calculations. *Physical Review B*, 84(8), 085204.
- 1163 [101] Zhang, W., Fisher, T. & Mingo, N. The atomistic Green's function method: An efficient
1164 simulation approach for nanoscale phonon transport. *Numerical Heat Transfer, Part B:*
1165 *Fundamentals* 51, 333-349 (2007).
- 1166 [102] S. Datta, *Electronic Transport in Mesoscopic Systems* (Cambridge University Press,
1167 1997).
- 1168 [103] Cepellotti, A., Fugallo, G., Paulatto, L., Lazzeri, M., Mauri, F., & Marzari, N. (2015).
1169 Phonon hydrodynamics in two-dimensional materials. *Nature communications*, 6(1), 1-7.
- 1170 [104] Lee, S., Broido, D., Esfarjani, K., & Chen, G. (2015). Hydrodynamic phonon transport
1171 in suspended graphene. *Nature communications*, 6(1), 1-10.
- 1172 [105] Lee, S., & Li, X. (2019). (invited book chapter) Hydrodynamic Phonon Transport: Past,
1173 Present, and Prospect. In *Nanoscale Energy Transport: Emerging Phenomena, Methods,*
1174 *and Applications*, Liao, B. (Ed.). Institute of Physics Publishing
- 1175 [106] Li, X., & Lee, S. (2019). Crossover of ballistic, hydrodynamic, and diffusive phonon
1176 transport in suspended graphene. *PHYSICAL REVIEW B*, 99(8).
- 1177 [107] Mezhev-Deglin, L. Measurement of the thermal conductivity of crystalline He4. *J. Exp.*
1178 *Theor. Phys.* 49, 66–79 (1965).
- 1179 [108] Huberman, S., Duncan, R. A., Chen, K., Song, B., Chiloyan, V., Ding, Z., ... & Nelson,
1180 K. A. (2019). Observation of second sound in graphite at temperatures above 100 K.
1181 *Science*, 364(6438), 375-379.
- 1182 [109] Shang, M. Y., Zhang, C., Guo, Z., & Lü, J. T. (2020). Heat vortex in hydrodynamic
1183 phonon transport of two-dimensional materials. *Scientific Reports*, 10(1), 1-10.
- 1184 [110] Wang, X. M., Mo, D. C., & Lu, S. S. (2013). On the thermoelectric transport properties
1185 of graphyne by the first-principles method. *The Journal of chemical physics*, 138(20),
1186 204704.
- 1187 [111] Gu, X., & Yang, R. (2016). Phonon transport and thermal conductivity in two-
1188 dimensional materials. *Annual Review of Heat Transfer*, 19.
- 1189 [112] W.J. Evans, L. Hu, and P. Keblinski, Thermal conductivity of graphene ribbons from
1190 equilibrium molecular dynamics: Effect of ribbon width, edge roughness, and hydrogen
1191 termination, *Appl. Phys. Lett.*, Vol. 96, p. 203112, 2010.

- 1192 [113] Feng, T., Ruan, X., Ye, Z., & Cao, B. (2015). Spectral phonon mean free path and thermal
1193 conductivity accumulation in defected graphene: The effects of defect type and
1194 concentration. *Physical Review B*, 91(22), 224301.
- 1195 [114] Girit, Ç. Ö., Meyer, J. C., Erni, R., Rossell, M. D., Kisielowski, C., Yang, L., Park, C.-
1196 H., Crommie, M., Cohen, M. L. & Louie, S. G. Graphene at the edge: stability and
1197 dynamics. *Science* 323, 1705-1708 (2009).
- 1198 [115] Z. Guo, D. Zhang, and X.-G. Gong, Thermal conductivity of graphene nanoribbons, *Appl.*
1199 *Phys. Lett.*, Vol. 95, p. 163103, 2009.
- 1200 [116] Munoz, E., Lu, J., & Yakobson, B. I. (2010). Ballistic thermal conductance of graphene
1201 ribbons. *Nano letters*, 10(5), 1652-1656.
- 1202 [117] Z. Wei, Y. Chen, and C. Dames, Wave packet simulations of phonon boundary scattering
1203 at graphene edges, *J. Appl. Phys.*, Vol. 112, p. 024328, 2012.
- 1204 [118] Ouyang, Y., & Guo, J. (2009). A theoretical study on thermoelectric properties of
1205 graphene nanoribbons. *Applied Physics Letters*, 94(26), 263107.
- 1206 [119] Sevinçli, H., & Cuniberti, G. (2010). Enhanced thermoelectric figure of merit in edge-
1207 disordered zigzag graphene nanoribbons. *Physical Review B*, 81(11), 113401.
- 1208 [120] Haskins, J., Kınacı, A., Sevik, C., Sevinçli, H., Cuniberti, G., & Çağm, T. (2011). Control
1209 of thermal and electronic transport in defect-engineered graphene nanoribbons. *ACS*
1210 *nano*, 5(5), 3779-3787.
- 1211 [121] Karamitaheri, H., Neophytou, N., Pourfath, M., Faez, R., & Kosina, H. (2012).
1212 Engineering enhanced thermoelectric properties in zigzag graphene nanoribbons. *Journal*
1213 *of Applied Physics*, 111(5), 054501.
- 1214 [122] Zheng, H., Liu, H. J., Tan, X. J., Lv, H. Y., Pan, L., Shi, J., & Tang, X. F. (2012).
1215 Enhanced thermoelectric performance of graphene nanoribbons. *Applied Physics Letters*,
1216 100(9), 093104.
- 1217 [123] Tran, V. T., Saint-Martin, J., Dollfus, P., & Volz, S. (2017). Optimizing the
1218 thermoelectric performance of graphene nanoribbons without degrading the electronic
1219 properties. *Scientific reports*, 7(1), 1-11.
- 1220 [124] Shihua Tan, Ke-Qiu Chen. The enhancement of the thermoelectric performance in zigzag
1221 graphene nanoribbon by edge states. *Carbon* 2015, 94, 942-945. DOI:
1222 10.1016/j.carbon.2015.07.083.
- 1223 [125] Sevinçli, H., Sevik, C., Çağm, T., & Cuniberti, G. (2013). A bottom-up route to enhance
1224 thermoelectric figures of merit in graphene nanoribbons. *Scientific reports*, 3(1), 1-6.
- 1225 [126] Pan, C. N., Xie, Z. X., Tang, L. M., & Chen, K. Q. (2012). Ballistic thermoelectric
1226 properties in graphene-nanoribbon-based heterojunctions. *Applied Physics Letters*,
1227 101(10), 103115.

- 1228 [127] Mazzamuto, F., Nguyen, V. H., Apertet, Y., Caër, C., Chassat, C., Saint-Martin, J., &
1229 Dollfus, P. (2011). Enhanced thermoelectric properties in graphene nanoribbons by
1230 resonant tunneling of electrons. *Physical Review B*, 83(23), 235426.
- 1231 [128] Yeo, P. S. E., Sullivan, M. B., Loh, K. P., & Gan, C. K. (2013). First-principles study of
1232 the thermoelectric properties of strained graphene nanoribbons. *Journal of Materials*
1233 *Chemistry A*, 1(36), 10762-10767.
- 1234 [129] Wei, N., Xu, L., Wang, H. Q., & Zheng, J. C. (2011). Strain engineering of thermal
1235 conductivity in graphene sheets and nanoribbons: a demonstration of magic
1236 flexibility. *Nanotechnology*, 22(10), 105705.
- 1237 [130] Liang, L., Cruz-Silva, E., Girão, E. C., & Meunier, V. (2012). Enhanced thermoelectric
1238 figure of merit in assembled graphene nanoribbons. *Physical Review B*, 86(11), 115438.
- 1239 [131] Mazzamuto, F., Saint-Martin, J., Nguyen, V. H., Chassat, C., & Dollfus, P. (2012).
1240 Thermoelectric performance of disordered and nanostructured graphene ribbons using
1241 Green's function method. *Journal of Computational Electronics*, 11(1), 67-77.
- 1242 [132] Yan, Y., Liang, Q. F., Zhao, H., & Wu, C. Q. (2012). Thermoelectric properties of
1243 hexagonal graphene quantum dots. *Physics Letters A*, 376(12-13), 1154-1158.
- 1244 [133] Ni, X., Liang, G., Wang, J. S., & Li, B. (2009). Disorder enhances thermoelectric figure
1245 of merit in armchair graphene nanoribbons. *Applied Physics Letters*, 95(19), 192114.
- 1246 [134] Yang, K., Cahangirov, S., Cantarero, A., Rubio, A., & D'Agosta, R. (2014).
1247 Thermoelectric properties of atomically thin silicene and germanene nanostructures.
1248 *Physical Review B*, 89(12), 125403.
- 1249 [135] Zborecki, K., Wierzbicki, M., Barnaś, J., & Swirkowicz, R. (2013). Thermoelectric
1250 effects in silicene nanoribbons. *Physical Review B*, 88(11), 115404.
- 1251 [136] Zborecki, K., Swirkowicz, R., & Barnaś, J. (2014). Spin effects in thermoelectric
1252 properties of Al- and P-doped zigzag silicene nanoribbons. *Physical Review B*, 89(16),
1253 165419.
- 1254 [137] Fan, D. D., Liu, H. J., Cheng, L., Jiang, P. H., Shi, J., & Tang, X. F. (2014). MoS₂
1255 nanoribbons as promising thermoelectric materials. *Applied Physics Letters*, 105(13),
1256 133113.
- 1257 [138] Chen, K. X., Luo, Z. Y., Mo, D. C., & Lyu, S. S. (2016). WSe₂ nanoribbons: new high-
1258 performance thermoelectric materials. *Physical Chemistry Chemical Physics*, 18(24),
1259 16337-16344.
- 1260 [139] Wang, J., Xie, F., Cao, X. H., An, S. C., Zhou, W. X., Tang, L. M., & Chen, K. Q. (2017).
1261 Excellent Thermoelectric Properties in monolayer WSe₂ Nanoribbons due to Ultralow
1262 Phonon Thermal Conductivity. *Scientific reports*, 7(1), 1-8.

- 1263 [140] Zhang, J., Liu, H. J., Cheng, L., Wei, J., Liang, J. H., Fan, D. D., ... & Zhang, Q. J. (2014).
 1264 Phosphorene nanoribbon as a promising candidate for thermoelectric applications.
 1265 Scientific reports, 4(1), 1-8.
- 1266 [141] Chen, X. K., Xie, Z. X., Zhou, W. X., Tang, L. M., & Chen, K. Q. (2016). Phonon wave
 1267 interference in graphene and boron nitride superlattice. Applied Physics Letters, 109(2),
 1268 023101.
- 1269 [142] Felix, I. M., & Pereira, L. F. C. (2018). Thermal conductivity of graphene-hBN
 1270 superlattice ribbons. Scientific reports, 8(1), 2737.
- 1271 [143] Tran, V. T., Saint-Martin, J., & Dollfus, P. (2015). High thermoelectric performance in
 1272 graphene nanoribbons by graphene/BN interface engineering. Nanotechnology, 26(49),
 1273 495202.
- 1274 [144] Yokomizo, Y., & Nakamura, J. (2013). Giant Seebeck coefficient of the graphene/h-BN
 1275 superlattices. Applied Physics Letters, 103(11), 113901.
- 1276 [145] Yang, K., Chen, Y., D'Agosta, R., Xie, Y., Zhong, J., & Rubio, A. (2012). Enhanced
 1277 thermoelectric properties in hybrid graphene/boron nitride nanoribbons. Physical Review
 1278 B, 86(4), 045425.
- 1279 [146] Zhang, Z., Xie, Y., Peng, Q., & Chen, Y. (2016). A theoretical prediction of super high-
 1280 performance thermoelectric materials based on MoS₂/WS₂ hybrid nanoribbons. Scientific
 1281 reports, 6, 21639.
- 1282 [147] Ouyang, Y., Xie, Y., Zhang, Z., Peng, Q., & Chen, Y. (2016). Very high thermoelectric
 1283 figure of merit found in hybrid transition-metal-dichalcogenides. Journal of Applied
 1284 Physics, 120(23), 235109.
- 1285 [148] Oswald W and Wu Z 2012 Energy gaps in graphene nanomeshes Phys. Rev. B 85 115431
- 1286 [149] Ouyang, F., Peng, S., Liu, Z., & Liu, Z. (2011). Bandgap opening in graphene antidot
 1287 lattices: the missing half. ACS nano, 5(5), 4023-4030.
- 1288 [150] Vanević, M., Stojanović, V. M., & Kindermann, M. (2009). Character of electronic states
 1289 in graphene antidot lattices: Flat bands and spatial localization. Physical Review B, 80(4),
 1290 045410.
- 1291 [151] Pedersen, T. G., Flindt, C., Pedersen, J., Mortensen, N. A., Jauho, A. P., & Pedersen, K.
 1292 (2008). Graphene antidot lattices: designed defects and spin qubits. Physical Review
 1293 Letters, 100(13), 136804.
- 1294 [152] Yang, L., Chen, J., Yang, N., & Li, B. (2015). Significant reduction of graphene thermal
 1295 conductivity by phononic crystal structure. International Journal of Heat and Mass
 1296 Transfer, 91, 428-432.
- 1297 [153] Tianli Feng, Xiulin Ruan. Ultra-low thermal conductivity in graphene nanomesh. Carbon
 1298 2016, 101, 107-113.

- 1299 [154] Gunst, T., Markussen, T., Jauho, A. P., & Brandbyge, M. (2011). Thermoelectric
1300 properties of finite graphene antidot lattices. *Physical Review B*, 84(15), 155449.
- 1301 [155] Karamitaheri, H., Pourfath, M., Faez, R., & Kosina, H. (2011). Geometrical effects on
1302 the thermoelectric properties of ballistic graphene antidot lattices. *Journal of Applied*
1303 *Physics*, 110(5), 054506.
- 1304 [156] Yan, Y., Liang, Q. F., Zhao, H., Wu, C. Q., & Li, B. (2012). Thermoelectric properties
1305 of one-dimensional graphene antidot arrays. *Physics Letters A*, 376(35), 2425-2429.
- 1306 [157] Hossain, M. S., Al-Dirini, F., Hossain, F. M., & Skafidas, E. (2015). High performance
1307 graphene nano-ribbon thermoelectric devices by incorporation and dimensional tuning of
1308 nanopores. *Scientific reports*, 5, 11297.
- 1309 [158] Chang, P. H., Bahramy, M. S., Nagaosa, N., & Nikolic, B. K. (2014). Giant
1310 thermoelectric effect in graphene-based topological insulators with heavy adatoms and
1311 nanopores. *Nano letters*, 14(7), 3779-3784.
- 1312 [159] Sadeghi, H., Sangtarash, S., & Lambert, C. J. (2015). Enhanced thermoelectric efficiency
1313 of porous silicene nanoribbons. *Scientific reports*, 5, 9514.
- 1314 [160] Shao, L., Chen, G., Ye, H., Wu, Y., Niu, H., & Zhu, Y. (2014). Theoretical study on
1315 electronic properties of MoS₂ antidot lattices. *Journal of Applied Physics*, 116(11),
1316 113704.
- 1317 [161] Cupo, A., Masih Das, P., Chien, C. C., Danda, G., Kharche, N., Tristant, D., ... & Meunier,
1318 V. (2017). Periodic arrays of phosphorene nanopores as antidot lattices with tunable
1319 properties. *ACS Nano*, 11(7), 7494-7507.
- 1320 [162] Yamawaki, M., Ohnishi, M., Ju, S., & Shiomi, J. (2018). Multifunctional structural
1321 design of graphene thermoelectrics by Bayesian optimization. *Science Advances*, 4(6),
1322 eaar4192.
- 1323 [163] Wei, H., Bao, H., & Ruan, X. (2020). Genetic algorithm-driven discovery of unexpected
1324 thermal conductivity enhancement by disorder. *Nano Energy*, 71, 104619.
- 1325 [164] Ju, S., Shiga, T., Feng, L., Hou, Z., Tsuda, K., & Shiomi, J. (2017). Designing
1326 nanostructures for phonon transport via Bayesian optimization. *Physical Review X*, 7(2),
1327 021024.
- 1328 [165] Wan, X., Feng, W., Wang, Y., Wang, H., Zhang, X., Deng, C., & Yang, N. (2019).
1329 Materials Discovery and Properties Prediction in Thermal Transport via Materials
1330 Informatics: A Mini Review. *Nano letters*, 19(6), 3387-3395.
- 1331 [166] Wang, T., Zhang, C., Snoussi, H., & Zhang, G. (2020). Machine Learning Approaches
1332 for Thermoelectric Materials Research. *Advanced Functional Materials*, 30(5), 1906041.
- 1333 [167] Wu, D., Yu, Z., Xiao, J., & Ouyang, F. (2010). The chemical modification of graphene
1334 antidot lattices. *Physica E: Low-dimensional Systems and Nanostructures*, 43(1), 33-39.

- 1335 [168] Liu, X., Zhang, Z., & Guo, W. (2013). Universal rule on chirality - dependent bandgaps
1336 in graphene antidot lattices. *Small*, 9(8), 1405-1410.
- 1337 [169] Ji, X., Zhang, J., Wang, Y., Qian, H., & Yu, Z. (2013). Influence of edge imperfections
1338 on the transport behavior of graphene nanomeshes. *Nanoscale*, 5(6), 2527-2531.
- 1339 [170] Dvorak, M., Oswald, W., & Wu, Z. (2013). Bandgap opening by patterning graphene.
1340 *Scientific reports*, 3(1), 1–7.
- 1341 [171] Brun, S. J., Thomsen, M. R., & Pedersen, T. G. (2014). Electronic and optical properties
1342 of graphene antidot lattices: comparison of Dirac and tight-binding models. *Journal of*
1343 *Physics: Condensed Matter*, 26(26), 265301.
- 1344 [172] Yuan, S., Roldán, R., Jauho, A. P., & Katsnelson, M. I. (2013). Electronic properties of
1345 disordered graphene antidot lattices. *Physical Review B*, 87(8), 085430.
- 1346 [173] Fürst, J. A., Pedersen, J. G., Flindt, C., Mortensen, N. A., Brandbyge, M., Pedersen, T.
1347 G., & Jauho, A. P. (2009). Electronic properties of graphene antidot lattices. *New Journal*
1348 *of Physics*, 11(9), 095020.
- 1349 [174] Hung Nguyen, V., Chung Nguyen, M., Nguyen, H.-V. & Dollfus, P. Disorder effects on
1350 electronic bandgap and transport in graphene-nanomesh-based structures. *Journal of*
1351 *Applied Physics* 113, 013702 (2013).
- 1352 [175] Kim, M., Safron, N. S., Han, E., Arnold, M. S. & Gopalan, P. Fabrication and
1353 characterization of large-area, semiconducting nanoporated graphene materials. *Nano*
1354 *letters* 10, 1125-1131 (2010).
- 1355 [176] Bai, J., Zhong, X., Jiang, S., Huang, Y. & Duan, X. Graphene nanomesh. *Nature*
1356 *nanotechnology* 5, 190-194 (2010).
- 1357 [177] Shi, L., Li, D., Yu, C., Jang, W., Kim, D., Yao, Z., ... & Majumdar, A. (2003). Measuring
1358 thermal and thermoelectric properties of one-dimensional nanostructures using a
1359 microfabricated device. *J. Heat Transfer*, 125(5), 881-888.
- 1360 [178] Kim, P., Shi, L., Majumdar, A., & McEuen, P. L. (2001). Thermal transport
1361 measurements of individual multiwalled nanotubes. *Physical review letters*, 87(21),
1362 215502.
- 1363 [179] Xu, X., Pereira, L. F., Wang, Y., Wu, J., Zhang, K., Zhao, X., ... & Hong, B. H. (2014).
1364 Length-dependent thermal conductivity in suspended single-layer graphene. *Nature*
1365 *communications*, 5(1), 1-6.
- 1366 [180] Jang, W., Bao, W., Jing, L., Lau, C. N., & Dames, C. (2013). Thermal conductivity of
1367 suspended few-layer graphene by a modified T-bridge method. *Applied Physics Letters*,
1368 103(13), 133102.
- 1369 [181] Jauregui, L. A., Yue, Y., Sidorov, A. N., Hu, J., Yu, Q., Lopez, G., Jalilian, R., Benjamin,
1370 D. K., Delkd, D. A. & Wu, W. Thermal transport in graphene nanostructures: Experiments
1371 and simulations. *Ecs Transactions* 28, 73-83 (2010).

- 1372 [182] Chen, S., Moore, A. L., Cai, W., Suk, J. W., An, J., Mishra, C., ... & Ruoff, R. S. (2011).
1373 Raman measurements of thermal transport in suspended monolayer graphene of variable
1374 sizes in vacuum and gaseous environments. *ACS nano*, 5(1), 321-328.
- 1375 [183] Sullivan, S., Vallabhaneni, A., Kholmanov, I., Ruan, X., Murthy, J., & Shi, L. (2017).
1376 Optical generation and detection of local nonequilibrium phonons in suspended graphene.
1377 *Nano letters*, 17(3), 2049-2056.
- 1378 [184] Xiao, N., Dong, X., Song, L., Liu, D., Tay, Y., Wu, S., ... & Huang, W. (2011). Enhanced
1379 thermopower of graphene films with oxygen plasma treatment. *ACS Nano*, 5(4), 2749-
1380 2755.
- 1381 [185] Oh, J., Yoo, H., Choi, J., Kim, J. Y., Lee, D. S., Kim, M. J., ... & Lee, S. S. (2017).
1382 Significantly reduced thermal conductivity and enhanced thermoelectric properties of
1383 single-and bi-layer graphene nanomeshes with sub-10 nm neck-width. *Nano Energy*, 35,
1384 26-35.
- 1385 [186] Dongchao Xu, Shuang Tang, Xu Du, Qing Hao, Detecting the Major Charge-Carrier
1386 Scattering Mechanism in Graphene Antidot Lattices, *Carbon* 144, 601-607 (2019).
- 1387 [187] Xu, D., Wang, Q., Wu, X., Zhu, J., Zhao, H., Xiao, B., ... & Hao, Q. (2018). Largely
1388 reduced cross-plane thermal conductivity of nanoporous In_{0.1}Ga_{0.9}N thin films directly
1389 grown by metal organic chemical vapor deposition. *Frontiers in Energy*, 12(1), 127-136.
- 1390 [188] Hu, S., Zhang, Z., Jiang, P., Ren, W., Yu, C., Shiomi, J., & Chen, J. (2019). Disorder
1391 limits the coherent phonon transport in two-dimensional phononic crystal structures.
1392 *Nanoscale*, 11(24), 11839-11846.
- 1393 [189] Liu, F., Wang, Z., Nakanao, S., Ogawa, S., Morita, Y., Schmidt, M., ... & Mizuta, H.
1394 (2020). Conductance Tunable Suspended Graphene Nanomesh by Helium Ion Beam
1395 Milling. *Micromachines*, 11(4), 387.
- 1396 [190] Wang, H., Kurata, K., Fukunaga, T., Takamatsu, H., Zhang, X., Ikuta, T., ... & Takata,
1397 Y. (2016). In-situ measurement of the heat transport in defect-engineered free-standing
1398 single-layer graphene. *Scientific reports*, 6(1), 1-7.
- 1399 [191] Kang, M. S., Kang, S. Y., Lee, W. Y., Park, N. W., Kwon, K. C., Choi, S., ... & Jang, H.
1400 W. (2020). Large-scale MoS₂ thin films with chemically formed holey structure for
1401 enhanced Seebeck thermopower and their anisotropic properties. *Journal of Materials*
1402 *Chemistry A*.
- 1403 [192] Li, Q. Y., Zhang, X., & Hu, Y. D. (2014). Laser flash Raman spectroscopy method for
1404 thermophysical characterization of 2D nanomaterials. *Thermochimica acta*, 592, 67-72.
- 1405 [193] Li, Q. Y., Ma, W. G., & Zhang, X. (2016). Laser flash Raman spectroscopy method for
1406 characterizing thermal diffusivity of supported 2D nanomaterials. *International Journal of*
1407 *Heat and Mass Transfer*, 95, 956-963.

- 1408 [194] Sullivan, S., Vallabhaneni, A., Kholmanov, I., Ruan, X., Murthy, J., & Shi, L. (2017).
1409 Optical generation and detection of local nonequilibrium phonons in suspended
1410 graphene. *Nano letters*, 17(3), 2049-2056.
- 1411 [195] Vallabhaneni, A. K., Singh, D., Bao, H., Murthy, J., & Ruan, X. (2016). Reliability of
1412 Raman measurements of thermal conductivity of single-layer graphene due to selective
1413 electron-phonon coupling: A first-principles study. *Physical Review B*, 93(12), 125432.
- 1414 [196] Li, Q. Y., Feng, T., Okita, W., Komori, Y., Suzuki, H., Kato, T., Kaneko, T., Ikuta, T.,
1415 Ruan, X., Takahashi, K. (2019). Enhanced Thermoelectric Performance of As-Grown
1416 Suspended Graphene Nanoribbons. *ACS Nano*, 13(8), 9182-9189.
- 1417 [197] Li, Q. Y., Takahashi, K., Ago, H., Zhang, X., Ikuta, T., Nishiyama, T., & Kawahara, K.
1418 (2015). Temperature dependent thermal conductivity of a suspended submicron graphene
1419 ribbon. *Journal of Applied Physics*, 117(6), 065102.
- 1420 [198] Md Sharafat Hossain, Duc Hau Huynh, Phuong Duc Nguyen, Liming Jiang, Thanh Cong
1421 Nguyen, Feras Al-Dirini, Faruque M. Hossain, Efstratios Skafidas. Enhanced
1422 thermoelectric performance of graphene nanoribbon-based devices. *Journal of Applied
1423 Physics* 2016, 119 (12), 125106. DOI: 10.1063/1.4944710.
- 1424 [199] Han, M. Y., Özyilmaz, B., Zhang, Y., & Kim, P. (2007). Energy band-gap engineering
1425 of graphene nanoribbons. *Physical review letters*, 98(20), 206805.
- 1426 [200] Bae, M. H., Li, Z., Aksamija, Z., Martin, P. N., Xiong, F., Ong, Z. Y., ... & Pop, E. (2013).
1427 Ballistic to diffusive crossover of heat flow in graphene ribbons. *Nature communications*,
1428 4(1), 1-7.
- 1429 [201] C. Kamal, M. Ezawa, Arsenene: Two-dimensional buckled and puckered honeycomb
1430 arsenic systems, *Phys. Rev. B - Condens. Matter Mater. Phys.* 91 (2015) 1–10.
1431 <https://doi.org/10.1103/PhysRevB.91.085423>.
- 1432 [202] Li, Q. Y., Zhang, X., & Takahashi, K. (2018). Variable-spot-size laser-flash Raman
1433 method to measure in-plane and interfacial thermal properties of 2D van der Waals
1434 heterostructures. *International Journal of Heat and Mass Transfer*, 125, 1230-1239.
- 1435 [203] Vaziri, S., Yalon, E., Rojo, M. M., Suryavanshi, S. V., Zhang, H., McClellan, C. J., ... &
1436 Deshmukh, S. (2019). Ultrahigh thermal isolation across heterogeneously layered two-
1437 dimensional materials. *Science advances*, 5(8), eaax1325.
- 1438 [204] Chen, C. C., Li, Z., Shi, L., & Cronin, S. B. (2015). Thermoelectric transport across
1439 graphene/hexagonal boron nitride/graphene heterostructures. *Nano Research*, 8(2), 666-
1440 672.
- 1441 [205] Mahapatra, P. S., Sarkar, K., Krishnamurthy, H. R., Mukerjee, S., & Ghosh, A. (2017).
1442 Seebeck coefficient of a single van der Waals junction in twisted bilayer graphene. *Nano
1443 letters*, 17(11), 6822-6827.

- 1444 [206] Poudel, N., Liang, S. J., Choi, D., Hou, B., Shen, L., Shi, H., ... & Cronin, S. (2017).
1445 Cross-plane thermoelectric and thermionic transport across Au/h-BN/graphene
1446 heterostructures. *Scientific reports*, 7(1), 1-8.
- 1447 [207] Chen, C. C.; Li, Z.; Shi, L.; Cronin, S. B. Thermal interface conductance across a
1448 graphene/hexagonal boron nitride heterojunction. *Appl. Phys. Lett.* 2014, 104, 081908.
- 1449 [208] Oh, J., Kim, Y., Chung, S., Kim, H., & Son, J. G. (2019). Fabrication of a MoS₂/Graphene
1450 Nanoribbon Heterojunction Network for Improved Thermoelectric Properties. *Advanced*
1451 *Materials Interfaces*, 6(23), 1901333.
- 1452 [209] Lee, C., Hong, J., Whangbo, M. H., & Shim, J. H. (2013). Enhancing the thermoelectric
1453 properties of layered transition-metal dichalcogenides 2H-MQ₂ (M= Mo, W; Q= S, Se,
1454 Te) by layer mixing: Density functional investigation. *Chemistry of Materials*, 25(18),
1455 3745-3752.
- 1456 [210] Wang, X., Zebarjadi, M., & Esfarjani, K. (2018). High-performance solid-state
1457 thermionic energy conversion based on 2D van der Waals heterostructures: A first-
1458 principles study. *Scientific reports*, 8(1), 1-9.
- 1459 [211] Ding, G., Wang, C., Gao, G., Yao, K., Dun, C., Feng, C., ... & Zhang, G. (2018).
1460 Engineering of charge carriers via a two-dimensional heterostructure to enhance the
1461 thermoelectric figure of merit. *Nanoscale*, 10(15), 7077-7084.
- 1462 [212] Snyder, G. J., & Snyder, A. H. (2017). Figure of merit ZT of a thermoelectric device
1463 defined from materials properties. *Energy & Environmental Science*, 10(11), 2280-2283.
- 1464 [213] J. Wu, Y. Liu, Y. Cai, Y. Zhao, H.K. Ng, K. Watanabe, T. Taniguchi, G. Zhang,
1465 C.-W. Qiu, D. Chi, A.H.C. Neto, J.T.L. Thong, K.P. Loh, K. Hippalgaonkar, Large
1466 enhancement of thermoelectric performance in MoS₂/h-BN heterostructure due to
1467 vacancy-induced band hybridization, *Proc. Natl. Acad. Sci.* (2020) 202007495.
1468 <https://doi.org/10.1073/pnas.2007495117>.
- 1469 [214] Ge, Y., Wan, W., Ren, Y., & Liu, Y. Large thermoelectric power factor of high-mobility
1470 1T" phase of transition-metal dichalcogenides. *PHYSICAL REVIEW RESEARCH* 2,
1471 013134 (2020)
- 1472 [215] Deng, S., Li, L., Guy, O. J., & Zhang, Y. (2019). Enhanced thermoelectric performance
1473 of monolayer MoSSe, bilayer MoSSe and graphene/MoSSe heterogeneous
1474 nanoribbons. *Physical Chemistry Chemical Physics*, 21(33), 18161-18169.
- 1475 [216] Dehkordi AM, Zebarjadi M, He J, Tritt TM (2015) Thermoelectric power factor:
1476 Enhancement mechanisms and strategies for higher performance thermoelectric materials.
1477 *Mater Sci Eng Rep* 97:1–22. 31.
- 1478 [217] Sadeghi, H., Sangtarash, S., & Lambert, C. J. (2016). Cross-plane enhanced
1479 thermoelectricity and phonon suppression in graphene/MoS₂ van der Waals
1480 heterostructures. *2D Materials*, 4(1), 015012.

- 1481 [218] Ding, Z., An, M., Mo, S., Yu, X., Jin, Z., Liao, Y., ... & Yang, N. (2019). Unexpectedly
1482 high cross-plane thermoelectric performance of layered carbon nitrides. *Journal of*
1483 *materials chemistry A*, 7(5), 2114-2121.
- 1484 [219] Olaya, D., Hurtado-Morales, M., Gómez, D., Castañeda-Urbe, O. A., Juang, Z. Y., &
1485 Hernández, Y. (2017). Large thermoelectric figure of merit in graphene layered devices at
1486 low temperature. *2D Materials*, 5(1), 011004.
- 1487 [220] Jia, P. Z., Zeng, Y. J., Wu, D., Pan, H., Cao, X. H., Zhou, W. X., ... & Chen, K. Q. (2019).
1488 Excellent thermoelectric performance induced by interface effect in MoS₂/MoSe₂ van der
1489 Waals heterostructure. *Journal of Physics: Condensed Matter*, 32(5), 055302.
- 1490 [221] Yalon, E., McClellan, C. J., Smithe, K. K., Muñoz Rojo, M., Xu, R. L., Suryavanshi, S.
1491 V., ... & Pop, E. (2017). Energy dissipation in monolayer MoS₂ electronics. *Nano*
1492 *letters*, 17(6), 3429-3433.
- 1493 [222] Hu, J., Wu, T., Tian, J., Klimov, N. N., Newell, D. B., & Chen, Y. P. (2017). Coulomb
1494 drag and counterflow Seebeck coefficient in bilayer-graphene double layers. *Nano*
1495 *Energy*, 40, 42-48.
- 1496 [223] X. Wang, M. Zebarjadi, K. Esfarjani, First principles calculations of solid-state
1497 thermionic transport in layered van der Waals heterostructures, *Nanoscale*. 8 (2016)
1498 14695–14704. <https://doi.org/10.1039/C6NR02436J>.
- 1499 [224] A. Shakouri, J.E. Bowers, Heterostructure integrated thermionic coolers, *Appl. Phys. Lett.*
1500 71 (1997) 1234. <https://doi.org/10.1063/1.119861>.
- 1501 [225] G.D. Mahan, J.O. Sofo, M. Bartkowiak, Multilayer Thermionic Refrigerator and
1502 Generator, *J. Appl. Phys.* 83 (1998) 17. <https://doi.org/10.1063/1.367255>.
- 1503 [226] G.D. Mahan, Thermionic refrigeration, *J. Appl. Phys.* 76 (1994) 4362–4366.
1504 <https://doi.org/10.1063/1.357324>.
- 1505 [227] G.O. Fitzpatrick, E.J. Britt, B. Moyzhes, Updated perspective on the potential for
1506 thermionic conversion to meet 21st Century energy needs, in: *IECEC-97 Proc. Thirty-*
1507 *Second Intersoc. Energy Convers. Eng. Conf. (Cat. No.97CH6203)*, IEEE, 1997: pp.
1508 1045–1051 vol.2. <https://doi.org/10.1109/IECEC.1997.661913>.
- 1509 [228] H. MOSS, Thermionic Diodes as Energy Converters, *J. Electron. Control.* 2 (1957) 305–
1510 322. <https://doi.org/10.1080/00207215708937036>.
- 1511 [229] K. G. Hernqvist; M. Kanefsky; F. H. Norman, Thermionic energy converter, *RCA. Rev.*
1512 19 (1958) 244–258.
- 1513 [230] M.G. Rosul, M.S. Akhanda, M. Zebarjadi, Thermionic energy conversion, in: *Nanoscale*
1514 *Energy Transp.*, IOP Publishing, 2020: pp. 14-1-14–29. [https://doi.org/10.1088/978-0-](https://doi.org/10.1088/978-0-7503-1738-2ch14)
1515 [7503-1738-2ch14](https://doi.org/10.1088/978-0-7503-1738-2ch14).

- 1516 [231] M. Zebarjadi, Solid-State Thermionic Power Generators: An Analytical Analysis in the
 1517 Nonlinear Regime, *Phys. Rev. Appl.* 8 (2017) 014008.
 1518 <https://doi.org/10.1103/PhysRevApplied.8.014008>.
- 1519 [232] X. Wang, M. Zebarjadi, K. Esfarjani, High-Performance Solid-State Thermionic Energy
 1520 Conversion Based on 2D van der Waals Heterostructures : A First-Principles Study, *Sci.*
 1521 *Rep.* 8 (2018) 1–9. <https://doi.org/10.1038/s41598-018-27430-0>.
- 1522 [233] S.-J. Liang, B. Liu, W. Hu, K. Zhou, L.K. Ang, Thermionic Energy Conversion Based
 1523 on Graphene van der Waals Heterostructures, *Sci. Rep.* 7 (2017) 46211.
 1524 <https://doi.org/10.1038/srep46211>.
- 1525 [234] H. Sadeghi, S. Sangtarash, C.J. Lambert, Cross-plane enhanced thermoelectricity and
 1526 phonon suppression in graphene/MoS₂ van der Waals heterostructures, *2D Mater.* 4 (2016)
 1527 015012. <https://doi.org/10.1088/2053-1583/4/1/015012>.
- 1528 [235] D.G. Cahill, Analysis of heat flow in layered structures for time-domain
 1529 thermoreflectance, *Rev. Sci. Instrum.* 75 (2004) 5119–5122.
 1530 <https://doi.org/10.1063/1.1819431>.
- 1531 [236] K.M. Freedy, T. Zhu, D.H. Olson, P.M. Litwin, P. Hopkins, M. Zebarjadi, S.J.
 1532 McDonnell, Interface chemistry and thermoelectric characterization of Ti and TiOx
 1533 Contacts to MBE-Grown WSe₂, *2D Mater.* (2020). [https://doi.org/10.1088/2053-](https://doi.org/10.1088/2053-1583/ab834b)
 1534 [1583/ab834b](https://doi.org/10.1088/2053-1583/ab834b).
- 1535 [237] M.G. Rosul, D. Lee, D.H. Olson, N. Liu, X. Wang, P.E. Hopkins, K. Lee, M. Zebarjadi,
 1536 Thermionic transport across gold-graphene-WSe₂ van der Waals heterostructures, *Sci.*
 1537 *Adv.* 5 (2019) eaax7827. <https://doi.org/10.1126/sciadv.aax7827>.
- 1538 [238] Lim, J., Wang, H. T., Tang, J., Andrews, S. C., So, H., Lee, J., ... & Yang, P. (2016).
 1539 Simultaneous thermoelectric property measurement and incoherent phonon transport in
 1540 holey silicon. *ACS nano*, 10(1), 124-132.
- 1541 [239] Mahmood, J., Lee, E. K., Jung, M., Shin, D., Jeon, I. Y., Jung, S. M., ... & Park, N. (2015).
 1542 Nitrogenated holey two-dimensional structures. *Nature communications*, 6(1), 1-7.
- 1543 [240] Mahmood, J., Lee, E. K., Jung, M., Shin, D., Choi, H. J., Seo, J. M., ... & Park, N. (2016).
 1544 Two-dimensional polyaniline (C3N) from carbonized organic single crystals in solid
 1545 state. *Proceedings of the National Academy of Sciences*, 113(27), 7414-7419.
- 1546 [241] Fischbein, M. D., & Drndić, M. (2008). Electron beam nanosculpting of suspended
 1547 graphene sheets. *Applied physics letters*, 93(11), 113107.
- 1548 [242] Russo, C. J., & Golovchenko, J. A. (2012). Atom-by-atom nucleation and growth of
 1549 graphene nanopores. *Proceedings of the National Academy of Sciences*, 109(16), 5953-
 1550 5957.
- 1551 [243] Dyck, O., Ziatdinov, M., Lingerfelt, D. B., Unocic, R. R., Hudak, B. M., Lupini, A. R., ...
 1552 & Kalinin, S. V. (2019). Atom-by-atom fabrication with electron beams. *Nature Reviews*
 1553 *Materials*, 4(7), 497-507.

- 1554 [244] Fujii, S., Yokoi, T., Fisher, C. A., Moriwake, H., & Yoshiya, M. (2020). Quantitative
1555 prediction of grain boundary thermal conductivities from local atomic environments.
1556 Nature communications, 11(1), 1-10.
- 1557 [245] Zhang, H., Hippalgaonkar, K., Buonassisi, T., Løvvik, O. M., Sagvolden, E., & Ding, D.
1558 Machine Learning for Novel Thermal-Materials Discovery: Early Successes,
1559 Opportunities, and Challenges. ES Energy Environ., 2018, 2, 1–8.
- 1560 [246] Lang Wu, Yue Xiao, M. Ghosh, Qiang Zhou, Qing Hao, “Machine Learning Prediction
1561 for Bandgaps of Inorganic Materials,” ES Mater. Manuf. 9, 3 (2020).
- 1562 [247] Mueller, T., Hernandez, A., & Wang, C. (2020). Machine learning for interatomic
1563 potential models. The Journal of Chemical Physics, 152(5), 050902.
- 1564 [248] Mortazavi, B., Podryabinkin, E. V., Roche, S., Rabczuk, T., Zhuang, X., & Shapeev, A.
1565 V. (2020). Machine-learning interatomic potentials enable first-principles multiscale
1566 modeling of lattice thermal conductivity in graphene/borophene heterostructures.
1567 Materials Horizons. <https://doi.org/10.1039/D0MH00787K>
- 1568 [249] Qian, X., Peng, S., Li, X., Wei, Y., & Yang, R. (2019). Thermal conductivity modeling
1569 using machine learning potentials: application to crystalline and amorphous silicon.
1570 Materials Today Physics, 10, 100140.